WAVELET DE-NOISING APPLIED TO VIBRATIONAL ENVELOPE ANALYSIS METHODS

by

Edward Max Bertot

A Thesis Submitted to the Faculty of

The College of Engineering and Computer Science

in Partial Fulfillment of the Requirements for the Degree of

Master of Science

Florida Atlantic University

Boca Raton, FL

May 2014

WAVELET DE-NOISING APPLIED TO VIBRATIONAL ENVELOPE ANALYSIS METHODS

by

Edward Max Bertot

This thesis was prepared under the direction of the candidate's thesis co-advisors, Dr. Taghi Khoshgoftaar and Dr. Pierre-Philippe Beaujean, Department of Computer and Electrical Engineering and Computer Science, and has been approved by the members of his supervisory committee. It was submitted to the faculty of the College of Engineering and Computer Science and was accepted in partial fulfillment of the requirements for the degree of Master of Science.

SUPERVISORY COMMITTEE:

Taghi Khoshgoftaar, Ph.D.
Thesis Co-Advisor

Pierre-Philippe Beaujean, Ph.D.
Thesis Co-Advisor

Nurgun Erdol, Ph.D.

Nurgun Erdol, Ph.D.
Chair, Department of Computer & Electrical Engineering and Computer Science

Mohammad Ilyas, Ph.D.
Dean, The College of Engineering and Computer Science

Deborah L. Floyd, Ed.D.
Interim Dean, Graduate College

April 11, 2014
Date

ACKNOWLEDGEMENTS

Firstly, I'd like to thank my advisor Dr. Beaujean for always demanding the most. Throughout your classes and meetings I conquered difficult concepts, and they will undoubtedly serve me endlessly throughout my career. Perhaps we will work together again in the future!

Dr. Vendittis – our conversations kept me on track, and I sincerely appreciated our meetings. Your input was invaluable to the direction of my studies.

Additionally I'd like to thank my committee members, Dr. Khoshgoftaar and Dr. Erdol for their recommendations, which have sharpened the focus of this paper.

I'd like to apologize to my friends Phillp, Larry, Paulie, Jate, Coco, Elena, Cait, and others, whom I neglected during the writing of this paper. I appreciate you infinitely, and will now be available to party more often.

My employers and friends Brian and Dana, for providing me with "work" during these difficult economic times. You allowed me to fund my engineering education in the most exciting way possible.

All my aunts Lisa, Titi, Alicia, Susan, and Astrid; your accomplishments are an endless source of inspiration!

Most of all, my mother, father, and sister - you provided support, encouragement, and love, even as I spent all day at the computer. I cannot overstate my appreciation, nor can I express the amount of love I have for you.

ABSTRACT

Author:	Edward Max Bertot
Title:	Wavelet De-Noising Applied to Vibrational Envelope Analysis Methods
Institution:	Florida Atlantic University
Thesis Co-Advisors:	Dr. Taghi Khoshgoftaar Dr. Pierre-Philippe Beaujean
Degree:	Master of Science
Year:	2014

In the field of machine prognostics, vibration analysis is a proven method for detecting and diagnosing bearing faults in rotating machines. One popular method for interpreting vibration signals is envelope demodulation, which allows a technician to clearly identify an impulsive fault source and its severity.

However *incipient* faults – faults in early stages – are masked by in-band noise, which can make the associated impulses difficult to detect and interpret. In this thesis, Wavelet De-Noising (WDN) is implemented after envelope-demodulation to improve accuracy of bearing fault diagnostics. This contrasts the typical approach of de-noising as a preprocessing step.

When manually measuring time-domain impulse amplitudes, the algorithm shows varying improvements in Signal-to-Noise Ratio (SNR) relative to background vibrational noise. A frequency-domain measure of SNR agrees with this result.

DEDICATION

To my late Abuelita, whose ability to love I aspire to possess.

WAVELET DE-NOISING APPLIED TO VIBRATIONAL ENVELOPE ANALYSIS METHODS

List of Figures ix

1 Introduction 1

1.1 Bearing Failure in Rotating Machines 1

1.2 Detection 1

1.2.1 Signal Characteristics 1

1.2.2 Envelope Analysis 2

1.3 Objective 2

1.4 Wavelet De-Noising 2

1.5 Paper Structure 3

2 Literature Review 4

2.1 The Wavelet De-Noising Algorithm 4

2.1.1 Mallat and Hwang 4

2.1.2 Donoho and Johnstone 5

2.2 De-Noising for PHM Applications 5

2.2.1 Qui, Lee, Lin, and Yu 5

2.2.2 WDN and Spectral Subtraction, Bozchalooi and Liang 7

2.2.3 WDN Depth Automation 7

2.2.4 Direct Demodulation Using the Wavelet Transform 8

3 Wavelet De-Noising . . . 9
3.1 Orthogonal Signal Expansions . . . 9
3.2 Lapped Orthogonal Block-Transforms . . . 10
3.2.1 Short-Time Fourier Transform (STFT) . . . 10
3.2.2 Drawbacks . . . 11
3.3 Wavelet Transform . . . 12
3.3.1 Kernel Scaling and Shifting . . . 12
3.3.2 Definition . . . 13
3.3.3 Kernel . . . 14
3.3.4 Mirror Filters . . . 14
3.4 Subband Decomposition . . . 15
3.4.1 Multi-Rate Signal Processing . . . 15
3.4.2 Frequency Domain Effects of Resampling . . . 15
3.4.3 Subband Tree Structures . . . 16
3.5 Linear Soft Thresholding . . . 17
3.6 Calculating Bearing Fault Frequencies . . . 19

4 Methodology . . . 21
4.1 Signal Flow . . . 21
4.1.1 Envelope Demodulation . . . 23
4.1.2 WDN Algorithm . . . 23
4.1.3 Detecting the Dominant Impact Frequency . . . 24
4.2 Initial Testing . . . 24
4.2.1 Synthesized Signals . . . 24
4.2.2 Real Signals . . . 28
4.3 Parametric Analysis . . . 29
4.3.1 Time-Domain SNR Measure . . . 29

4.3.2 Threshold vs. Decomposition Level 30
4.3.3 Threshold vs. Wavelet 32

5 Results 34
5.1 Synthetic Impulses 34
5.1.1 Frequency-Domain Detection 34
5.1.2 Time-Domain Detection 36
5.1.3 Remarks 36
5.2 DC Motor 40
5.2.1 Frequency-Domain Detection 41
5.2.2 Time-Domain Detection 42
5.2.3 Remarks 42
5.3 Case Western Vibration Dataset 44
5.3.1 Frequency-Domain Results 45
5.3.2 Time-Domain Results 45
5.3.3 Remarks 46

6 Conclusions 47
6.1 Future Work 49

A Daubechies Wavelets 50

B Filter Design for Envelope Demodulation 54

C Test Platforms and Equipment 55

Bibliography 58

LIST OF FIGURES

3.1 Octave-band sampling grid for a 3-level decomposition. The frequency response of the relevant filterbank is shown in Appendix A for various Daubechies wavelets. 13

3.2 Octave subband tree structure with three levels of decomposition. The scale-space distribution is shown in Figure 3.1. If this pattern is repeated until cD_6 and cA_6, the 6-level decomposition shown in Figure 3.3 will result. 16

3.3 Wavelet decomposition six levels deep, using the db6 wavelet. Note the logarithmic frequency scale. This corresponds to the sampling grid shown in Figure 3.1, and the signal-flow diagram shown in Figure 3.2. 17

3.4 Full binary subband tree with three levels of decomposition. 18

3.5 A soft thresholding function. Note all inputs below the threshold λ are set to zero. 19

3.6 Cross-sectional schematic of a typical rolling-element bearing. 20

4.1 System flowchart for de-noised envelope analysis. The following sections contain detailed information for each block. 22

4.2 Synthesized Test Waveforms 25

4.3 The scale-space representation of a 10-level wavelet decomposition of a chirp using db6 wavelet. The original signal is a 20,000 sample sine sweep on the frequency interval $0 \leq \omega \leq 10000$ rad/sec, as shown in Figure 4.2. 26

4.4 The *blocks* function and WGN, SNR $\approx$ 8dB, de-noised using the Haar wavelet (db1) at 4 levels of decomposition. Discontinuities are preserved while removing high-frequency noise. 27

4.5 A threshold sweep for various decomposition levels, db6 wavelet. Synthetic envelope signal from Figure 5.1. Data polynomial-fitted for $R^2 > 80\%$. Useful values lie on $0.5 \leq k \leq 1.5$. 31

4.6 A threshold sweep for various wavelet choices. Synthetic envelope signal from Figure 5.1, 6 levels of decomposition. Data polynomial-fitted for $R^2 > 80\%$. 33

5.1 WGN added to damped sine pulses. To measure SNR (-0.6dB), the clean signal in the first plot is truncated to f_s/γ (one time-constant). The fourth and fifth plots show an increase in SNR_T by $\approx +1$dB from applying WDN. The benefits of this procedure are not immediately obvious in the time-domain. Wavelet decomposition using db20 wavelet at a depth of 10 levels. 35

5.2 Welch PSD of signals shown in Figure 5.1 (before/after WDN). Gray area shows $\pm 10\%$ of possible frequencies 36

5.3 Estimated fault frequency vs. threshold level for the noisy pulse signal shown in 5.1, periodic at 20Hz. By thresholding the peaks of this envelope at a variable level α, the de-noised envelope signal is shown to more accurately reflect periodicity at the fault frequency. 37

5.4 Histogram of impulse frequencies, before WDN. These values are derived from the threshold shown in Figure 5.6. Low frequency content is a result of the threshold missing lower-amplitude peaks. 38

5.5 Histogram of impulse frequencies, after WDN. With the same threshold as Figure 5.4, more peaks are included in the measure, at the proper fault frequency (around 20Hz). 39

5.6 A threshold set too high results in peaks being discarded from the first plot, whereas the WDN version of the signal still contains these peaks. 39

5.7 Time-domain waveform of DC-motor vibration signal at all stages of the algorithm. 40

5.8 An isolated waveform peak. Before de-noising (top), $\text{SNR}_T \approx 18.3$dB. After de-noising (bottom), $\text{SNR}_T \approx 19.9$dB. 41

5.9 Welch PSD of signals shown in Figure 5.7 (before/after WDN). Gray area shows $\pm 10\%$ of possible fault frequencies 42

5.10 Estimated fault frequency vs. threshold level for the vibration signal shown in 5.7. By thresholding the peaks of this envelope at a variable level α, the de-noised envelope signal is shown to more accurately reflect periodicity at the fault frequency for lower variation in α. . . . 43

5.11 The time-domain waveform of a seeded fault with 0.007" diameter in the outer-raceway at all stages of the algorithm. Data from [12]. . . 44

5.12 Low frequency PSD of the vibration signal shown in Figure 5.11. The fault frequency BPFO is approximately 107Hz. 45

5.13 Estimated fault frequency vs. threshold level for the vibration signal shown in 5.11. This figure demonstrates the importance of removing in-band harmonics from envelope signals. 46

A.1 Haar wavelet. 51

A.2 Magnitude-squared response of a 3-level decomposition using the Haar basis. 51

A.3 db6 wavelet. 52

A.4 db6 magnitude-squared response. 52

A.5 db20 wavelet. 53

A.6 db20 magnitude-squared response. 53

C.1 Published data setup from [12]. 56

C.2 DC motor test platform. 57

C.3 Close-up view of RPM sensor, vibration sensor, bearing, and drive shaft. 57

Chapter 1

Introduction

1.1 BEARING FAILURE IN ROTATING MACHINES

In a rotating mechanical systems, bearings are components most vulnerable to physical wear. Exposed to radial loading, bearings defer frictional forces via rolling elements. Bearings inevitably fail, and these failures manifest themselves as cracks or pits in rolling ball raceways, broken cages, or damaged rollers.

1.2 DETECTION

1.2.1 Signal Characteristics

In the field of Prognostics and Health Monitoring (PHM), different methods are commonly employed for faulty bearing detection. A faulty bearing will typically create periodic, impulsive vibrations, which are proportional to rotational speed. These vibrations may be recorded and analyzed to reveal the nature of a given fault. Systems with multiple bearings and gear reduction systems will exhibit unique fault frequencies due to varying component diameters and operating speeds. This simple observation may be exploited to determine exactly which component is failing. In more sophisticated systems, multiple sensors are often used to indicate fault locations based on local vibration power levels [7] [6].

1.2.2 Envelope Analysis

Within a given structure, fault-induced impulses will amplitude-modulate mechanical resonances [9]. Research on which this thesis is based [7] utilizes envelope analysis to extract impulses from the modulated signal, which allows for quick diagnosis of *apparent* mechanical problems.

However, *incipient* faults are rather difficult to detect using this method, due to low signal-to-noise ratio (SNR). Extraneous noise sources such as nearby modal resonances, vibrational reflections, and vibrational harmonics corrupt the envelope signal. This inevitably degrades early-detection abilities, and in turn deteriorates estimates of Remaining Useful Life (RUL). These sources are in-band and non-white, so their removal is less than trivial.

1.3 OBJECTIVE

To combat a low SNR in the demodulated signal, we require a "de-noising" technique. This research focuses on *wavelet de-noising* and its use in vibration analysis, particularly as a post-processing scheme for envelope analysis. A secondary objective is to reduce user-interaction with the algorithm's parameters to obtain beneficial results.

1.4 WAVELET DE-NOISING

Many techniques have been devised for noise removal via signal processing. For our purposes, the algorithm must process non-stationary signals with decent time-resolution. Vibration statistics will be in constant flux, given changes in bearing wear, speed, and operating environment. More importantly, it must perform without *a priori* knowledge of the noise.

As far as these requirements specify, wavelet techniques are proven candidates.

The wavelet transform outperforms the Short-Time Fourier Transform (STFT) in terms of temporal resolution, allowing it greater flexibility in analyzing non-stationary signals [10]. It has also been demonstrated that Wavelet De-Noising (WDN) requires no knowledge of the noise level in order to optimally remove it [3].

Further discussed in Section 2, another wavelet technique, *wavelet filtering* is used for impulse extraction. Though this procedure also uses wavelets, it is functionally different from the thresholding method described in [2]. Only a single filter structure is used, which must directly correlate with the fault impulse.

1.5 PAPER STRUCTURE

Chapter 2 contains previous literature pertaining to the WDN algorithm and its applications to machine prognostics. Following this, Chapter 3 is a technical overview of the WDN algorithm. This chapter also contains a short review of fault frequencies. Chapter 4 details the reasoning and procedures for testing WDN on synthetic and real data. Results are shown in Chapter 5 with brief commentary. The conclusions of this thesis are stated in Chapter 6. This chapter also gives recommendations for future direction of the research.

Chapter 2

Literature Review

2.1 THE WAVELET DE-NOISING ALGORITHM

2.1.1 Mallat and Hwang

In 1992, Mallat and Hwang [1] demonstrated a novel de-noising technique using wavelets. In their paper, a wavelet transform is performed, bringing the signal into the scale-space domain. Coefficients in this domain are removed such that only local modulus maxima are kept. The signal is then reconstructed with the new coefficients, which produced a de-noised version of the original signal.

A prominent advantage of their method (over other noise-removal techniques of the time) is the preservation of singularities in the new signal. In terms of a 1-dimensional signal, "singularities" refer to irregular structures or transient phenomena, such as discontinuities or amplitude spikes. For many applications, singularities contain important information about the underlying physical process, yet are often buried in noise.

Interestingly, the authors estimate the signal's temporal regularity using Lipschitz constants (a measure of the signal's continuity), then use this value to adjust the amplitude of the local maxima in the wavelet domain. They demonstrate that the recalculated wavelet coefficients provide enough information to approximately reconstruct the de-noised signal with most errors concentrated in the higher frequencies.

2.1.2 Donoho and Johnstone

A few years later, Donoho and Johnstone [2] published an improved procedure for coefficient scaling which utilizes *wavelet shrinkage*. Once the signal is transformed into the scale-space domain, the authors apply a soft-threshold function to the coefficient amplitudes. Essentially, this removes negligible values while retaining significant ones. As compared with the procedure described in [1], soft-thresholding is far less destructive.

This algorithm has advantages that make it hugely effective when dealing with a wide range of signals. In a mathematical dissection of wavelet domain thresholding, Donoho [3] lays a theoretical foundation for de-noising applications. He shows that nearly optimal noise filtering is achieved using the soft-threshold function. Importantly, his proofs demonstrate that the algorithmic implementation does not require *a priori* knowledge of the noise level. Donoho and Johnstone are widely cited as the creators of the common WDN algorithm.

2.2 DE-NOISING FOR PHM APPLICATIONS

2.2.1 Qui, Lee, Lin, and Yu

In a more recent publication, Qui et al. [6] apply wavelet domain techniques to the problem of vibration analysis. They experiment with two related techniques for interpreting noising signals: Wavelet filtering and WDN.

Wavelet Filtering

This technique is essentially a narrowband filtering using a properly constructed wavelet. The wavelet is chosen based on similarity to a characteristic impulsive vibration, or fault signature. The authors compare a mechanical impulse with the

real-valued Morlet wavelet.

A two step approach is used to appropriately adjust Morlet filter characteristics. First, the sparsity of the filtered signal, measured by its Shannon entropy, is tested as a function of β, or "shape factor". The value for β that provides the highest measure of sparsity (lowest entropy) is the optimal solution. Second, the authors use singular value decomposition (SVD) to test the periodicity of the filtered signal at various values of wavelet dilation, a.

Optimized wavelet filtering in this fashion is a good strategy, but requires some tuning and recursion to place β and a at useful values.

Wavelet De-Noising

The authors also use the method described in [2], discussed in Chapter 3, without any parameterizations or optimizations. They criticize the use of WDN for this application due to tuning difficulties:

> [...] there are other factors influencing the effectiveness of [wavelet] de-noising, such as the wavelet decomposition level and threshold rescaling method selection, which make the de-noising problem even more intricate. Since there are no explicit guidelines for how to tune the existing parameters, most of the time de-noising becomes a trial-and-error process. [6, pg. 1080]

There is much truth to this criticism, and using WDN on raw vibrational signals generally gives unpredictable results.

Relevant Conclusions

The authors conclude that WDN is unfit to be applied to impulsive vibrations:

> When dealing with smooth signals, satisfactory results can generally be achieved by manipulating the [soft-] threshold [value]. The underlying reason is because with smooth signals, a small number of large coefficients can charecterize the original signal. However, it is much more challenging to de-noise impulse series signals where wavelet coefficients are not so concentrated. [6, pg. 1088]

Which leads into the investigation this thesis provides. The Hilbert demodulation process inherently smooths vibration signals, so WDN will function more effectively. A secondary objective of this research is to reduce the amount of parameters necessary to tune the algorithm to a functional state for vibration analysis.

2.2.2 WDN and Spectral Subtraction, Bozchalooi and Liang

Bozchalooi and Liang [11] revisit the work of [6], improving the previous algorithm using spectral subtraction prior to wavelet filtering. To implement this, the power spectral density of the noise is estimated, then removed from the raw vibration signal. As a signal conditioning stage prior to other analyses, the authors demonstrate an improved reduction of in-band white Gaussian noise. Wavelet filtering, as in [6], then isolates a frequency of interest, exposing possible faults.

2.2.3 WDN Depth Automation

In a recent paper by Wald, Khoshgoftaar, and Sloan [8], the WDN algorithm's depth is automated using feature selection techniques. In this thesis, this parameter (n_d) is chosen as the maximum depth without further automation, a technique which sometimes results in large volumes of data. This is not an issue if window sizes are small, but large windows may require this type of technique, especially if real-time analysis is a requirement.

2.2.4 Direct Demodulation Using the Wavelet Transform

A notable application of the wavelet transform is its ability to directly demodulate a bandpass signal, as demonstrated by Nikolaou and Antoniadis [18]. For a given signal f, the modulus of its wavelet transform is the bandpass envelope.

$$|W_f^{a,s}(b)| = \sqrt{Re(W_f^{a,s}(b))^2 + Im(W_f^{a,s}(b))^2} \tag{2.1}$$

This particular property of the wavelet transform is not exploited in this thesis, but is discussed later in this report for future work.

Chapter 3

Wavelet De-Noising

Discussing multiresolution decomposition at depth first requires a few basic results. A good introduction is found in [5], and the same approach is taken here. Since decompositions are computed algorithmically, expressions are given in discrete form.

3.1 ORTHOGONAL SIGNAL EXPANSIONS

We begin the mathematical discussion with the expansion of a sampled signal into a weighted sum of component sequences. To create these component sequences, we require a set of *basis functions*, which will be multiplied with the original signal. The resulting component sequences will contain the original information that correlates with each basis function.

We desire these new sequences to be orthogonal so that the expansion contains no redundant information. We also wish that our basis functions are normalized so that there is no scaling. Essentially, we require an *orthonormal family* of functions.

Mathematically, the inner-product between any two different members of an orthonormal family is zero, and the inner product between two identical members results in 1. To illustrate this property, consider that the inner-product space between all members of an orthonormal family is the Kronecker delta matrix, as shown in

equation (3.1),

$$\langle \phi | \phi \rangle = \sum_{k=0}^{N-1} \phi_n[k] \phi_s^*[k] = \delta_{ns} \tag{3.1}$$
$$\text{for } 0 \leq n \leq N-1 \text{ and } 0 \leq s \leq N-1.$$

Here, variables n and s index the orthonormal family ϕ, which contains N linearly independent sequences. k is the discrete-time index.

The orthogonal expansion of a signal $f(k)$ can then be uniquely represented by a weighted sum, given by equation (3.2).

$$f[k] = \sum_{n=0}^{N-1} a_n \phi_n[k] \tag{3.2}$$
$$\text{for } 0 \leq k \leq N-1.$$

The values a_n may be referred to as "spectral coefficients".

As a related and familiar example, the Discrete Fourier Transform (DFT) is constructed using the orthogonal basis functions *sin* and *cos*, or more commonly in $\mathbb{C}$, the complex exponential function:

$$\phi[k] = e^{\frac{j2\pi rk}{N}} \tag{3.3}$$
$$\text{for } 0 \leq r \leq N-1.$$

Here, r represents the discrete frequency index. Sinusoidal transforms such as the DFT form the basis of harmonic analysis. They have proven invaluable in many applications, though notable drawbacks exist.

3.2 LAPPED ORTHOGONAL BLOCK-TRANSFORMS

3.2.1 Short-Time Fourier Transform (STFT)

To perform a time-varying analysis, a signal expansion may be executed on blocks of data which are spaced in time – *windows*. Probably the most widely used is the

Short Time Fourier Transform (STFT), which performs a DFT on windows which are linearly spaced in time. The result of this transformation is a time-frequency representation of the original signal.

$$F[m, \omega] = \sum_{n=0}^{N-1} f[n]w[n-m]e^{-j\omega n} \tag{3.4}$$

Here, w is a window, which is a function with relatively compact support. Multiplication with this window provides a small section of signal on which to perform the DFT. m is the sample delay of the window, which parameterizes time. ω is the normalized circular frequency,

$$\omega = 2\pi \frac{f}{f_s} \tag{3.5}$$

where f_s is the sampling frequency.

Window-overlap is achieved when the delay m is smaller than the length of the window function. This allows for a smoother temporal image, at the cost of redundancy. As the overlap is increased, the frequency domain is "smeared" over time.

3.2.2 Drawbacks

Fixed Time-Frequency Tiling

Due to the fixed length of the window function, each DFT will be computed identically. This results in linearly-spaced circular frequency bins from $0 \leq \omega \leq 2\pi$. Also, due to the fixed sample delay of the window functions, the time-resolution is also fixed and linear for all circular frequencies.

Gabor Limit

The most widely discussed obstacle in dealing with block transforms – and the STFT in particular – is the Gabor Limit. Intuitively, *a function cannot be limited in both*

time and frequency. If we window a function to gain temporal perspective, we increase the bandwidth in the frequency domain. If we increase the size of the window to reduce bandwidth, localization in time becomes difficult.

3.3 WAVELET TRANSFORM

3.3.1 Kernel Scaling and Shifting

A family of wavelet functions is defined by scaling and shifting – respectively a and b,

$$\psi_{a,b}(t) = \frac{1}{\sqrt{a}}\psi\left(\frac{t-b}{a}\right) \tag{3.6}$$

where ψ is a prototype function, or kernel, which is discussed in the following sections.

The scaling parameter will inherently construct a family of functions characterized by either:

- high-frequency, short-timescale
- low-frequency, long-timescale

This enables good localization of high-frequency events in time, while still allowing adequate integration times for low frequency events.

The proper selection of scaling values leads to logarithmically spaced frequency-bins; most naturally occurring signals are best represented via a frequency-logarithmic analysis [10]. The DFT, on the other hand, results in linearly spaced frequency bins. In order to represent such data logarithmically, an uneven redistribution is required along the frequency axis.

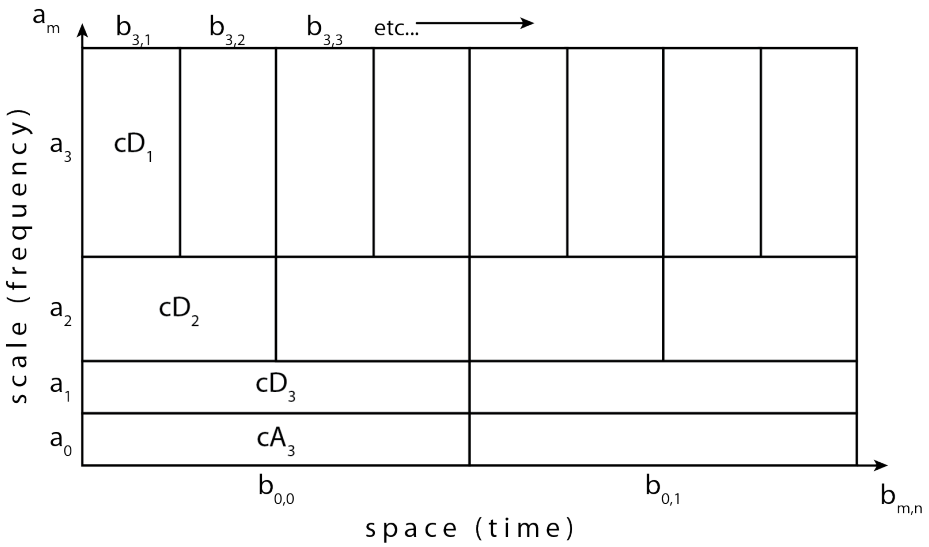

Figure 3.1: Octave-band sampling grid for a 3-level decomposition. The frequency response of the relevant filterbank is shown in Appendix A for various Daubechies wavelets.

3.3.2 Definition

The wavelet transform is easily visualized in the continuous domain:

$$W_f(a,b) = \int_{-\infty}^{\infty} f(t)\psi_{a,b}(t)dt \tag{3.7}$$

where $f(t)$ is an arbitrary function to be transformed.

In order to utilize this transform for sampled data, we discretize the scaling and shifting parameters on a *sampling grid* in the following manner:

$$a_m = a_0^m \tag{3.8}$$

$$b_{m,n} = nb_0a_0^m \tag{3.9}$$

Notably, the shifting parameter b is a function of scale a. This illustrates a crucial advantage of the Discrete Wavelet Transform (DWT); the distribution of information in frequency is *dyadic*, or *octave-band*. For analyzing natural signals, this is highly useful [10]. The scale-space tiling is shown in Figure 3.1.

The DWT results in a set of wavelet coefficients, which are given by the inner product

$$d_{m,n} = \langle f(t), \psi_{m,n}(t) \rangle \tag{3.10}$$

3.3.3 Kernel

Different from STFT kernels – which have fixed support and variable frequency – wavelet kernels have a support which is proportional to frequency, as dictated by translation/dilation.

Essentially a bandpass filter, wavelet kernels also have a quadrature mirror dual filter. This function acts as the lowpass complement to the wavelet, and is called the *scaling function* ϕ. During a wavelet decomposition, successively lower-frequency bandpass filters (wavelets) are used to orthogonally decompose the signal, and the lowest band is analyzed by the scaling function, which acts to "cap off" the low-end of the spectrum with a lowpass filter.

3.3.4 Mirror Filters

Given a real Finite Impulse Response (FIR) low-pass filter $h_L(n)$, its mirror is defined as:

$$h_H(n) = (-1)^n h_L(n)$$

Notably, these filters are frequency-symmetric about $\omega = \pi/2$, and are therefore commonly referred to as a quadrature mirror filter (QMF) pair. These symmetrical filters are useful for implementing filter banks, where the high- and lowpass filters split the signal into subbands of equal energies.

From a filter bank perspective, Daubechies wavelets are defined as maximally-flat QMF pairs. Their flatness is particularly useful for subband analysis, where a ripple in the passband would provide undesirable gains to scale-space coefficients. Appendix A

shows Daubechies wavelets of varying length and their respective frequency responses in a filter bank context.

3.4 SUBBAND DECOMPOSITION

3.4.1 Multi-Rate Signal Processing

Resampling is the modification of a signal's sampling rate. The procedures *downsampling* and *upsampling* – also known as *decimation* and *interpolation* – refer to the removal or insertion of samples, respectively. In both cases we choose an integer M as the resampling factor. Interpolation will insert $M-1$ points between each sample. Decimation will retain every M^{th} sample, discarding the others. Schematically, they are represented by "$\downarrow M$" (downsampling) and "$\uparrow M$" (upsampling).

3.4.2 Frequency Domain Effects of Resampling

Whenever modifying sample frequencies, the effects of aliasing must be countered. In both up- and downsampling, anti-aliasing filters are used to remove high frequency artifacts.

In the downsampling case, the signal is *compressed* in time by n/M, thus the scaling-property of the Fourier transform dictates a *stretching* in frequency by fM. Information within the circular frequency interval $[0, \pi/M]$ stretches to cover $[0, \pi]$. In order to prevent higher frequencies from reflecting into the baseband, a LPF is typically implemented at π/M prior to downsampling.

The upsampling case is the inverse: the signal is stretched in time by nM and compressed in frequency by f/M. Since the operation inserts M zeros between each sample, a set of high-frequency images is generated. A LPF at π/M is used after upsampling to remove these images and smooth the signal.

3.4.3 Subband Tree Structures

For each level of decomposition, new branches are added to the graph-theoretic "sub-band tree". In essence, the tree structure depicts how each frequency band is broken down into sub-bands. If QMF pairs are used to parse the spectrum, then *binary trees* can be used to represent the overall filtering scheme; each frequency band may potentially be reduced to an upper and lower subband.

Wavelet Decomposition Tree

A standard wavelet decomposition tree contains subbands which are logarithmically spaced in frequency. This implies a binary subband tree in which each low-frequency branch is split into another set of high/low branches, as shown in Figure 3.2. The resulting subbands are octave-related. A 6-level decomposition frequency response is shown in Figure 3.3.

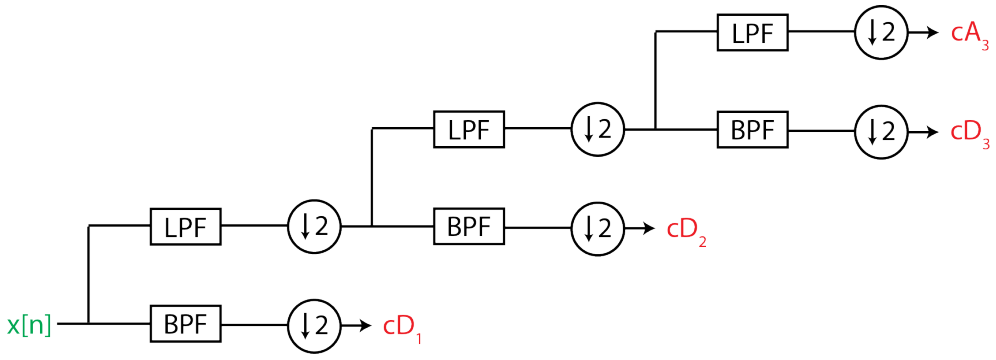

Figure 3.2: Octave subband tree structure with three levels of decomposition. The scale-space distribution is shown in Figure 3.1. If this pattern is repeated until cD_6 and cA_6, the 6-level decomposition shown in Figure 3.3 will result.

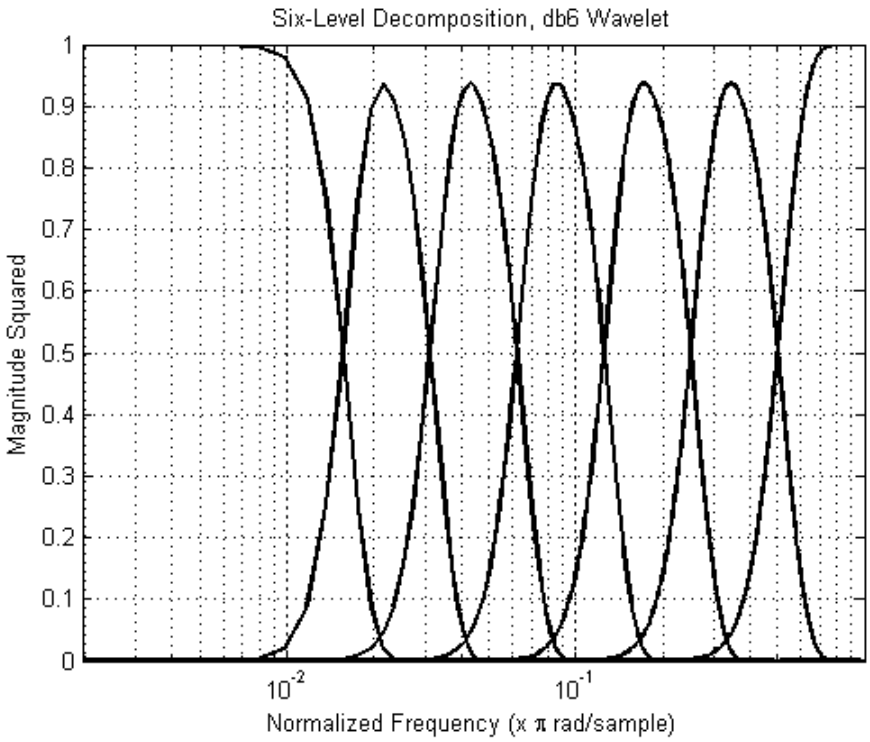

Figure 3.3: Wavelet decomposition six levels deep, using the db6 wavelet. Note the logarithmic frequency scale. This corresponds to the sampling grid shown in Figure 3.1, and the signal-flow diagram shown in Figure 3.2.

Wavelet Packet Decomposition Tree

A full decomposition, or packet decomposition, is a full binary tree (to a given depth). Each band is split successively into a high/low frequency subband pair. This decomposition provides a very rich analysis, and the tree is shown in Figure 3.4. This algorithm requires more computational power, and provides a linear frequency analysis.

3.5 LINEAR SOFT THRESHOLDING

As originally proposed by Donoho and Johnstone [2], the linear soft thresholding function is applied directly to the wavelet coefficients in the scale-space domain. This

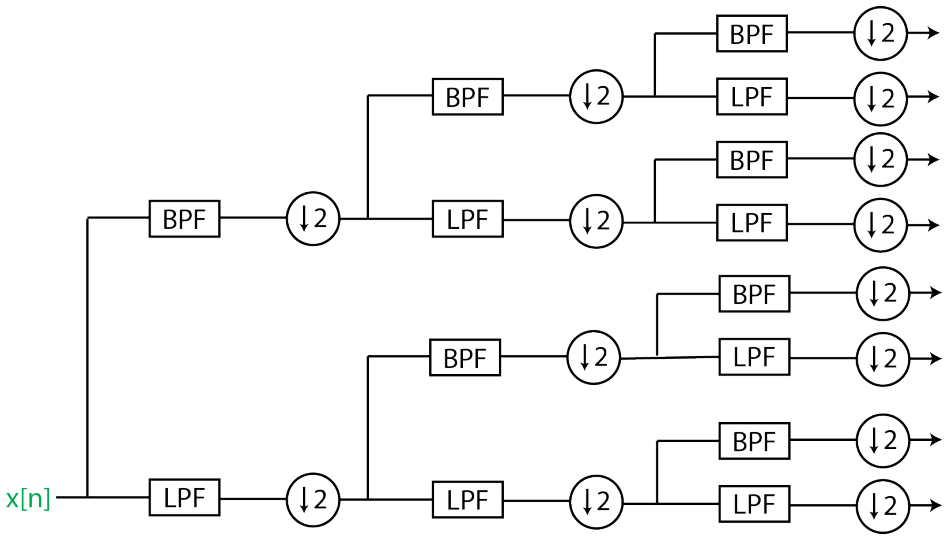

Figure 3.4: Full binary subband tree with three levels of decomposition.

piecewise defined function is given by

$$\tau(x) = \begin{cases} x - \lambda \text{sgn}(x), & |x| \geq \lambda \\ 0, & |x| < \lambda \end{cases} \tag{3.11}$$

where x are the values being thresholded, $\text{sgn}(x)$ is the sign of x, and λ is the threshold below which values are set to zero. Figure 3.5 shows an example soft-thresholding function.

The authors demonstrated that the threshold λ for near-optimality (in the minimax sense) is calculated as

$$\lambda = \sigma_x \sqrt{2 \log N} \tag{3.12}$$

where N is the number of samples in the time series and σ_x is the noise deviation. Exact noise statistics are difficult to estimate without *a priori* characteristics or reference measurements. Luckily for our applications, the noise dominates the signal, and we assume it is relatively Gaussian. Therefore, the noise deviation is just the

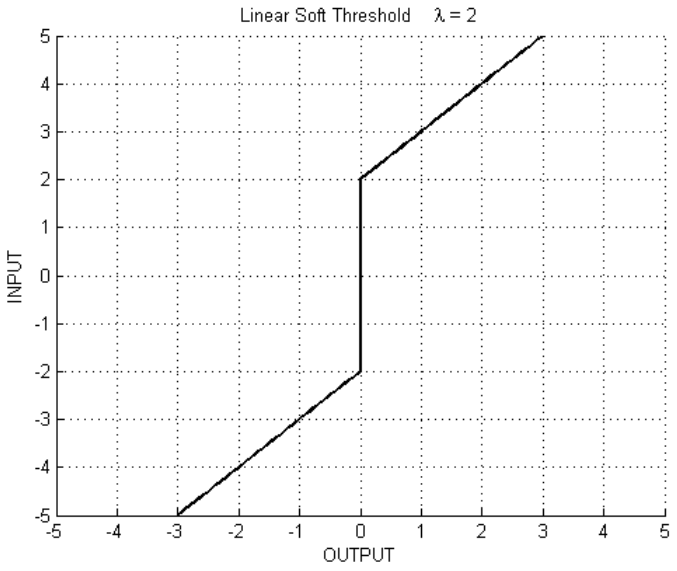

Figure 3.5: A soft thresholding function. Note all inputs below the threshold λ are set to zero.

deviation of the input signal.

$$\sigma_x \approx \sqrt{\frac{1}{N-1}\sum_{k=1}^{N}(x_k - \mu_x)^2} \tag{3.13}$$

where x_k are sample values and μ_x is the arithmetic mean of the time series.

For situational optimization, we multiply λ by a scaling value k to parameterize the threshold, as a sort of "twiddle" factor. Initial experiments have shown that this scale factor is generally acceptable at $k = 1$, but values $0.5 \leq k \leq 1.5$ may improve/degrade performance depending on the signal.

3.6 CALCULATING BEARING FAULT FREQUENCIES

Characteristic frequencies associated with the dimensions of a bearing can be used to pinpoint sources of vibration. The main components of a rolling-element bearing are the inner raceway, outer raceway, cage, and rolling elements. Figure 3.6 shows a cross-sectional sketch of a ball bearing, and the following equations relate rotational

frequency to fault frequencies.

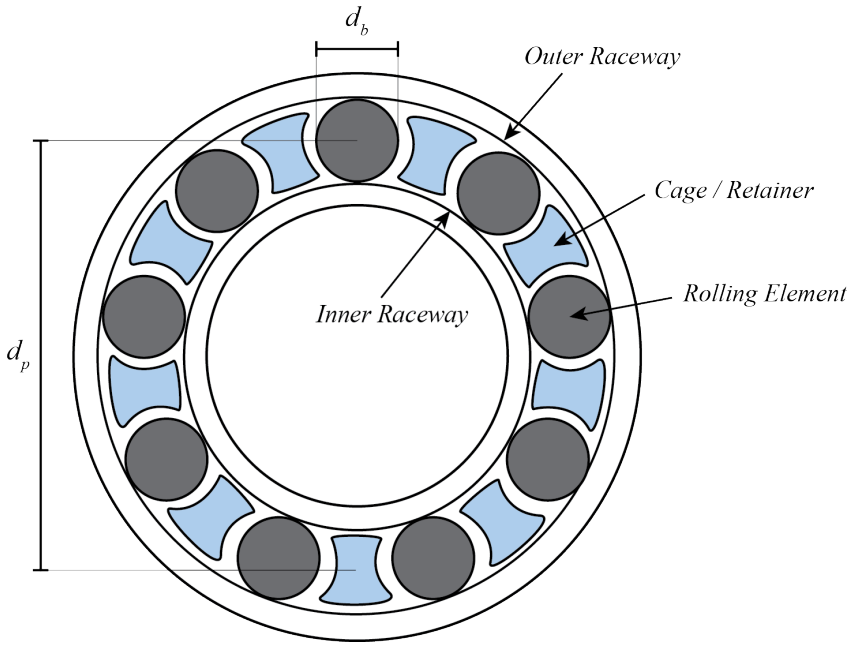

Figure 3.6: Cross-sectional schematic of a typical rolling-element bearing.

The ball spin frequency (BSF), or ball defect frequency

$$\text{BSF} = \frac{d_p}{2d_b} f_r \left(1 - \left(\frac{d_b}{d_p}\right)^2 \cos^2 \phi\right) \tag{3.14}$$

The Ball Pass Frequency Outer raceway (BPFO)

$$\text{BPFO} = \frac{n}{2} f_r \left(1 - \frac{d_b}{d_p} \cos \phi\right) \tag{3.15}$$

The Ball Pass Frequency Inner raceway (BPFI)

$$\text{BPFI} = \frac{n}{2} f_r \left(1 + \frac{d_b}{d_p} \cos \phi\right) \tag{3.16}$$

The Train Defect frequency (TD)

$$\text{TD} = \frac{1}{2} f_r \left(1 - \frac{d_b}{d_p} \cos \phi\right) \tag{3.17}$$

where f_r is the rotational speed, n is the number of balls, d_p is the pitch diameter, d_b is the ball diameter, and ϕ is the contact angle. [13]

Chapter 4

Methodology

4.1 SIGNAL FLOW

The demodulation procedure used in previous research by Waters and Beaujean [7] [16] is used to extract the envelope of the original vibration signal. A bandpass filter (BPF) is applied, where the center frequency is a structural mode of vibration. The Hilbert transform is then used to demodulate the bandpass signal into the baseband.

A multilevel wavelet decomposition is performed, which maps the signal into a set of coefficients in the scale-space domain. The coefficients are thresholded, as described by Donoho [3], which removes uncorrelated noise from the signal. The signal is then recomposed into the time domain, resulting in a *de-noised envelope* signal.

To extract fault frequencies, the periods between envelope peaks are measured and averaged over the length of the signal. The general signal flow chart is shown in Figure 4.1; all algorithms are implemented in MATLAB®.

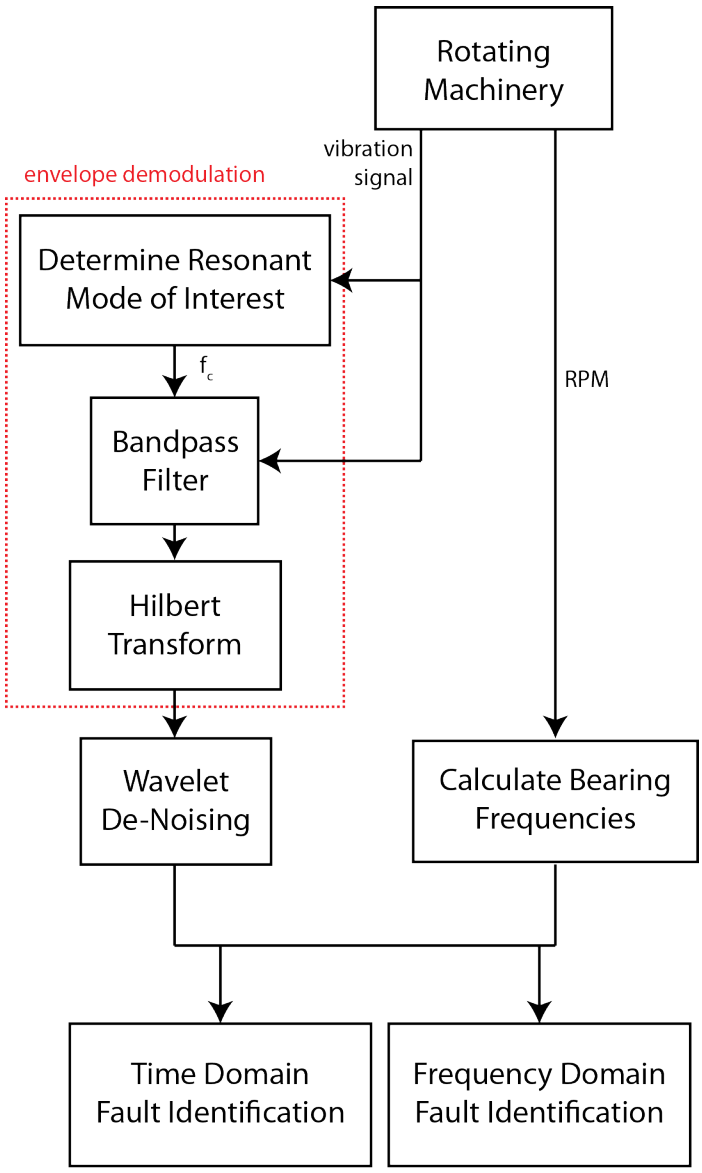

Figure 4.1: System flowchart for de-noised envelope analysis. The following sections contain detailed information for each block.

4.1.1 Envelope Demodulation

Finding the Vibrational Modes

To determine the vibrational modes of the structure, a Welch PSD is calculated to find a peak in the frequency spectrum, f_c. The Welch method provides an average over smaller time windows, so that spurious vibrations will not influence the selection of f_c. Different mechanical structures have different modes of vibration, so that f_c will vary depending on the setup.

Bandpass Filtering

A bandpass filter is designed centered on f_c (the chosen spectral peak). The filter is a Butterworth type to limit passband ripple, and is designed using the `fdesign` function in MATLAB's Filter Design Toolbox. The code to create the filter is listed in Appendix B.

Demodulation

The Hilbert transform is calculated using the `hilbert()` function, which demodulates the bandpass signal into the baseband. Spectral leakage from adjacent vibrational modes into the passband is the main source of noise.

4.1.2 WDN Algorithm

Now equipped with impact envelopes, a wavelet decomposition is performed using the `wavedec()` function, as described in Section 3.3. In the scale-space domain, a soft threshold is applied according to Eq. 3.11, which removes small-valued coefficients while preserving larger ones. The `waverec()` (wavelet reconstruction) function is used to bring the de-noised signal back into the time-domain. After the signal is

demodulated and de-noised, the SNR_T (defined in 4.3.1) is calculated to test the effectiveness of the algorithm.

4.1.3 Detecting the Dominant Impact Frequency

Following WDN, fault identification is attempted. In order to detect the proper fault frequency, methods are borrowed from [7].

A peak detector is used to find local maxima in the envelope signal. These peaks are thresholded at thr_e, which is a function of the average signal power,

$$thr_e = \alpha \frac{1}{N_e} \sum_{i=0}^{N_e-1} e_i^2. \tag{4.1}$$

where N_e is the number of samples in the envelope signal e. The constant α allows for adjustment to this threshold. This function will remove smaller peaks that are not associated with larger impacts.

The times between all successive peaks in the envelope signal are measured, resulting in a vector of impulse periods. The inverse of this vector is a set of impulse frequencies. A histogram will reveal higher concentrations on fault frequencies.

4.2 INITIAL TESTING

4.2.1 Synthesized Signals

To demonstrate and visualize the effects of de-noising, a set of typical synthetic waveforms was used. Taswell [19] attempted to standardize these functions for the purpose of de-noising algorithm benchmarking, and the generating functions can be found there. Waveforms are generated in MATLAB, and shown in Figure 4.2.

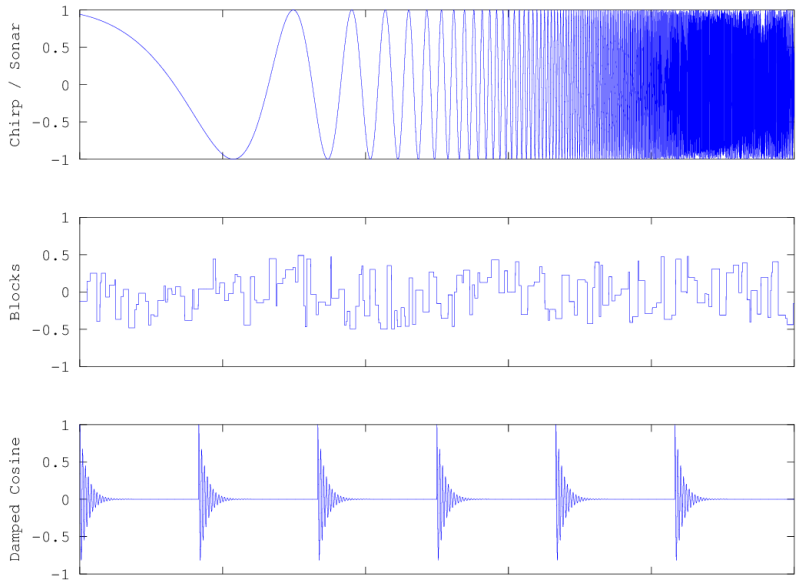

Figure 4.2: Synthesized Test Waveforms

Chirp

Pure signals are modeled with a *chirp* function (a.k.a. log-swept sine, doppler, or sonar). This shows how well a pure-tone signal is de-noised at all frequencies. It is also useful to demonstrate scale-space coefficients in a visual manner. Figure 4.3 shows a 10-level decomposition of the chirp function.

Blocks

The *blocks* signal is a randomized square wave with uniformly distributed duty cycle and amplitude. It demonstrates time-domain effects at discontinuities very clearly. The parameters are given as

$$\text{block width (samples)} = \texttt{round(100*rand(1,1))}$$

$$\text{amplitude} = \texttt{rand(1,1)-0.5}.$$

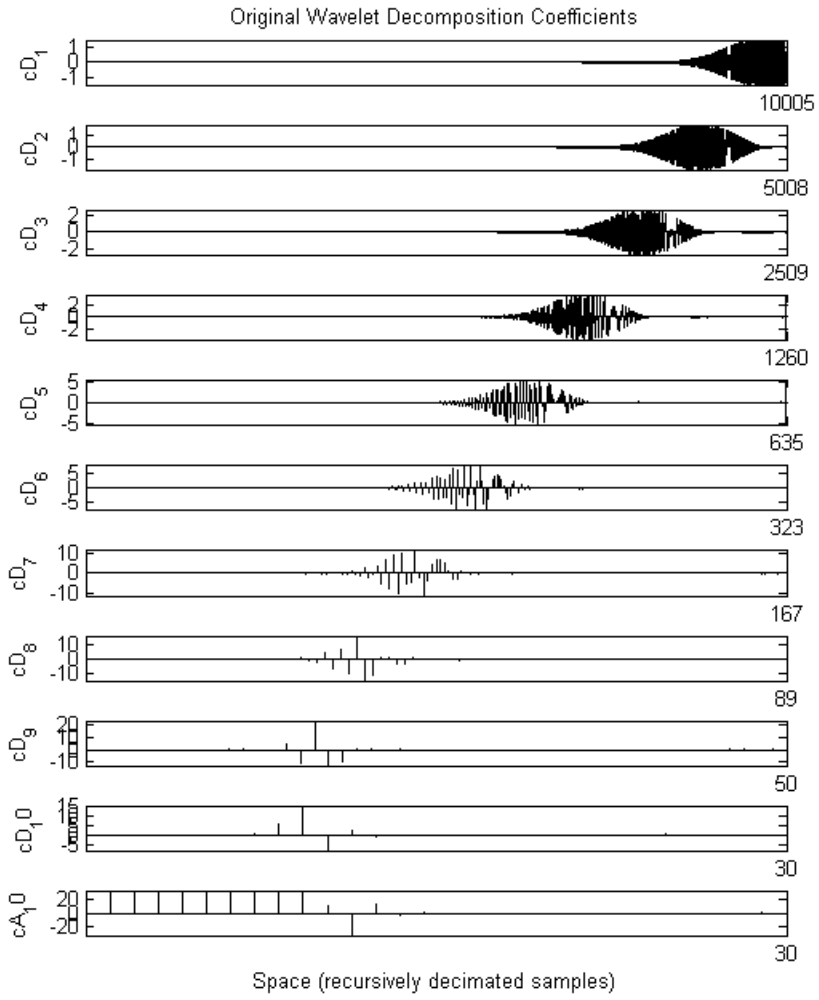

Figure 4.3: The scale-space representation of a 10-level wavelet decomposition of a chirp using db6 wavelet. The original signal is a 20,000 sample sine sweep on the frequency interval $0 \leq \omega \leq 10000$ rad/sec, as shown in Figure 4.2.

Square (constant) signals may be effectively decomposed by the Haar wavelet. This wavelet is shown in Appendix A and is used in Figure 4.4 to de-noise the blocks signal.

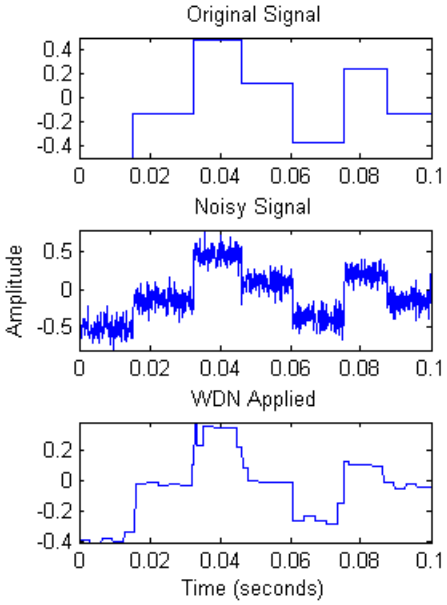

Figure 4.4: The *blocks* function and WGN, SNR $\approx$ 8dB, de-noised using the Haar wavelet (db1) at 4 levels of decomposition. Discontinuities are preserved while removing high-frequency noise.

Damped Sine

Finally and most applicably, a *damped sine* is used to model impulsive vibrations, similar to an excited structural resonance.

$$d[n] = e^{-\gamma\tau} sin(\omega\tau) \tag{4.2}$$

$$\tau = \frac{n}{f_s} \tag{4.3}$$

n is the sample number, f_s is the sampling frequency, τ is time relative to $n = 0$, and ω is the simulated resonant frequency (rad/sec). γ is the exponential decay constant,

which was chosen based on visual comparisons to a real-world signal. This function is windowed and repeated in time to simulate a periodic impact, much like a bearing fault may produce in rotating machinery. Values for modeling the signal in Section 5.3 are $\gamma \approx 1000$ and $\omega \approx 5000\pi$ rad/sec, where $f_s = 48$kHz.

4.2.2 Real Signals

DC Motor Testbed

This device was assembled in order to have a small test apparatus on-hand for rapid testing. It consists of a small 12V DC motor that drives a bearing mounted to an aluminum block, as shown in Figure C.2. Half of the shaft was painted to absorb light from an infrared reflectivity sensor; this outputs a square wave when the motor is running, which is effectively a rotational speed measurement. A closer view is shown in Figure C.3.

Used bearings were inserted into the aluminum block and vibration measurements were collected by a single accelerometer mounted perpendicular to the shaft.

The signal is sampled at 10kHz using LabVIEW IOtech data capture hardware. The vibration sensor used for this application is the CTC AC136 Low Frequency Accelerometer. It responds to frequencies up to 3kHz ($\pm$3dB), and has a dynamic range of $\pm$10g.

Case Western Dataset

The Case Western dataset is accessible to the public Internet at [12]. The setup is shown in Figure C.1, which shows a motor driven fan. The data includes bearing specifications, rotation speed, and fault specification. "Bearings were seeded with faults using Electro-Discharge Machining (EDM). Faults ranging from 0.007 inches in

diameter to 0.040 inches in diameter were introduced separately at the inner raceway, rolling element, and outer raceway." [12, Apparatus/Procedures page] The sampling frequency is 48kHz.

4.3 PARAMETRIC ANALYSIS

As Qui et al. [6] mention, WDN is an intricate algorithm with numerous parameters. Before applying WDN to real signals, the parameters are tested using the synthetic damped sine signal from Figure 5.1. Parametric sweeps were performed to test the effects of certain variables, namely:

- threshold λ
- wavelet type ψ
- decomposition level n_d

Most effective is the threshold λ, which is calculated as a function of signal variance (see Eq. 3.12). It may be slightly tweaked to obtain better results. Therefore, λ is used as the independent variable in these parameterizations. This value is tested against both n_d and ψ.

4.3.1 Time-Domain SNR Measure

To measure the effects of WDN parameters, SNR_T is used as a metric. For this calculation, the time-domain signal is visually scanned for a set of maxima (fault impulses). The power ratio between these impulses and surrounding "noise" samples is the estimated SNR, given by

$$\text{SNR}_T = 10 \log \frac{\frac{1}{N_S} \sum_{i=0}^{N_S-1} S_i^2}{\frac{1}{N_R} \sum_{j=0}^{N_R-1} R_i^2} \tag{4.4}$$

where N_S is the length of the identified impulse portion, N_R is the length of the surrounding noise portion. S and R are vectors containing concatenated impulse and noise envelopes, respectively. The length of these envelopes are determined by inspection, and are concatenated to remove zeros between occurrences.

4.3.2 Threshold vs. Decomposition Level

Figure 4.5 shows a variable scaling of λ by a *sensitivity factor* k for different levels of decomposition using the db6 wavelet.

As the algorithm removes more scale-space coefficients (increasing $k\lambda$), an eventuality is the removal of desired signal. The fitted curves in figure 4.5 shows a sharp increase in SNR due to the noise measure approaching zero. The problem with choosing values in this range is that most of the smaller signal peaks have been removed as well. Therefore the drastic increases in SNR are just an artifact of the measurement method. The default $k = 1$ is a safe choice, since the behavior of WDN becomes erratic (in terms of SNR) for larger values.

A limiting factor in decomposition is finite signal length. Shorter signals are limited in the number of decomposition levels possible, since each level of decomposition reduces the number of samples by half. For this reason, increasing decomposition depth is not always possible.

For example, a 5,000 point signal with 10 levels of decomposition will only contain $\frac{5000}{2^{10}} = 4$ coefficients in the cD_{10} and cA_{10} nodes, according to Figure 3.2. The lowest node (cA_{10}) will contain information on the normalized frequency interval $0 \leq \omega \leq \frac{\pi}{2^{10}} \frac{rad}{sample}$.

Converting from normalized units for a sample rate of $f_s = 10$kHz gives a lowpass

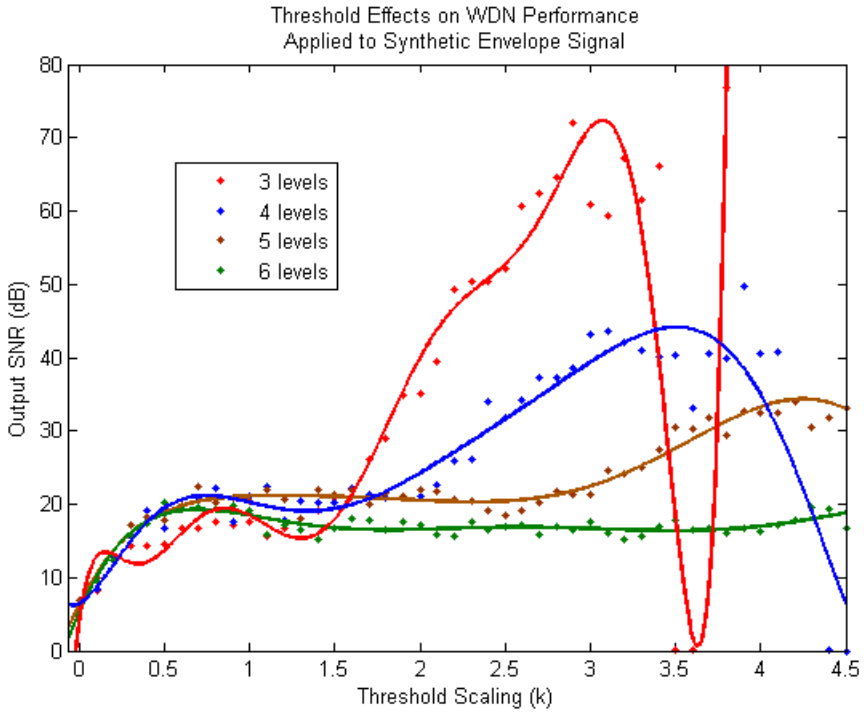

Figure 4.5: A threshold sweep for various decomposition levels, db6 wavelet. Synthetic envelope signal from Figure 5.1. Data polynomial-fitted for $R^2 > 80\%$. Useful values lie on $0.5 \leq k \leq 1.5$.

filter (scaling function ϕ) cutoff of

$$f_c = f_s \frac{\omega}{2\pi} = 1.5\text{Hz} \tag{4.5}$$

For baseband envelopes, the number of decompositions depends on the highest signal frequency. In the case of a rolling element bearing, it is BPFI, given by Equation 3.16. Therefore, to determine the maximum number of decompositions allowable, we find n_d such that

$$f_s \frac{\pi/2^{n_d}}{2\pi} > \text{BPFI}. \tag{4.6}$$

This will ensure that the frequencies of interest are not lost between subbands. The value BPFI is a function of rotational speed, as shown in Section 3.6.

4.3.3 Threshold vs. Wavelet

In Figure 4.6, λ is varied against three different wavelets (shown in Appendix A). Higher-order wavelets decrease subband leakage, but require more computational power. By decreasing subband leakage, narrowband signals have lesser chance of falling between subbands. In this case, energy is divided between subbands, and there is an increased likelihood of the signal being thresholded.

From the SNR_T measure alone, the results of using higher-order wavelets are not observed. It is straightforward to hypothesize the effects wavelet choice may have, and Section 5 confirms these deductions:

The signals involved in this research are *baseband envelopes*, which resemble a lowpass-filtered impulse train. In the frequency domain, this corresponds to high energy concentrations in lower frequencies, decreasing monotonically to the Hilbert filter bandwidth. Higher order wavelets will more accurately de-noise and reconstruct the low frequency band, which contains frequencies of interest.

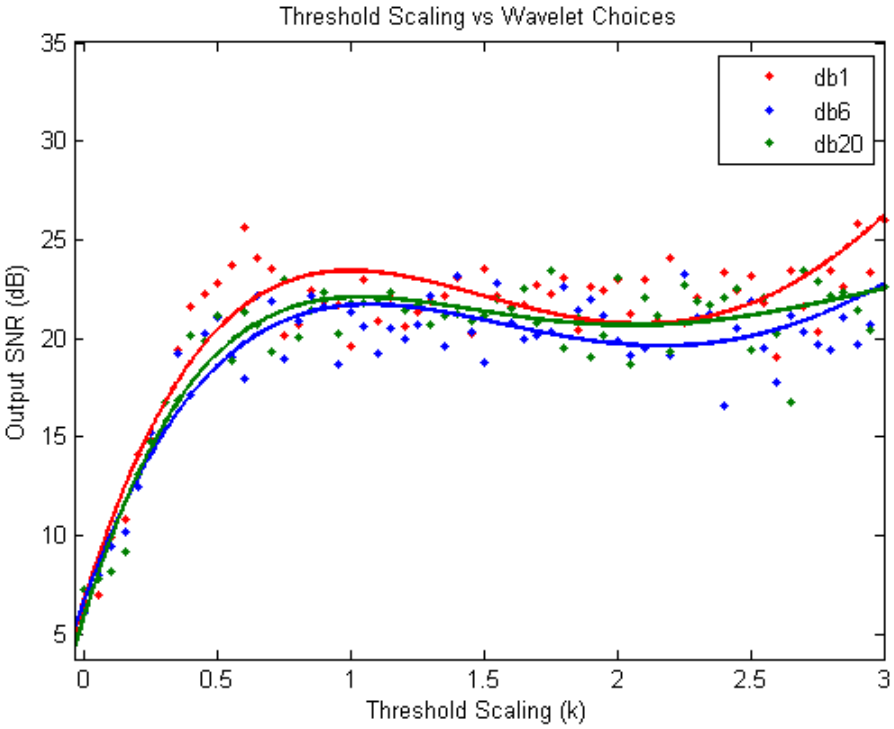

Figure 4.6: A threshold sweep for various wavelet choices. Synthetic envelope signal from Figure 5.1, 6 levels of decomposition. Data polynomial-fitted for $R^2 > 80\%$.

Chapter 5

Results

5.1 SYNTHETIC IMPULSES

The damped sine described in Section 4.2.1 is a controlled scenario, used to analyze the signal at all stages of the algorithm. A time-domain plot is shown in Figure 5.1.

To de-noise the envelope (baseband) signal, chosen parameters are the db20 wavelet with 10 levels of decomposition. The reasoning, using Equation 4.6, is that 10 levels of decomposition will give a lowpass (scaling filter) cutoff at $\approx$ 24Hz. This cutoff needs to be set above the BPFI of any bearings in question, since this is the highest fault frequency possible. Any lower, and fault frequencies may be split between subbands. The synthetic fault frequency is 20Hz.

5.1.1 Frequency-Domain Detection

Figure 5.2 shows a low-frequency Welch PSD of the signal before and after WDN, with the speculated fault frequencies (BSF, BPFO, BPFI) in grey. Without WDN applied, higher harmonics dominate the signal, which decreases the likelihood of proper fault identification.

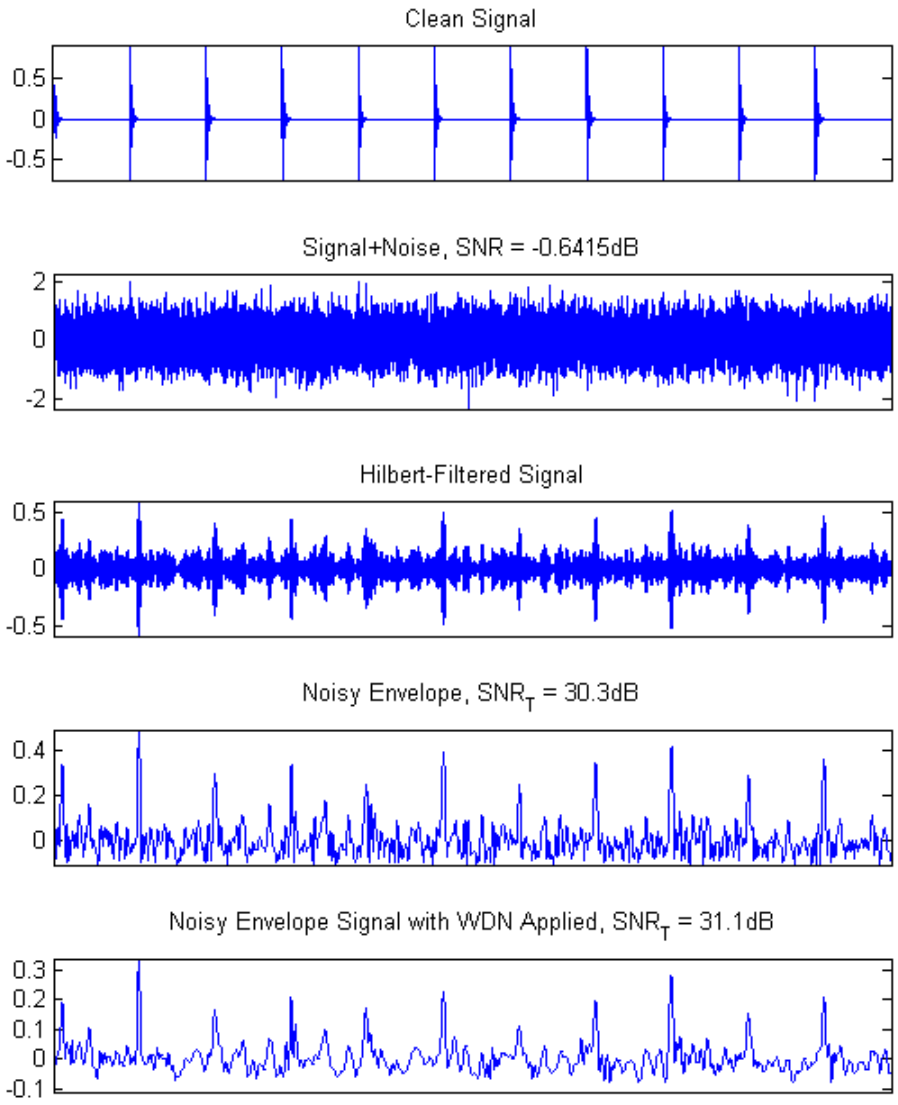

Figure 5.1: WGN added to damped sine pulses. To measure SNR (-0.6dB), the clean signal in the first plot is truncated to f_s/γ (one time-constant). The fourth and fifth plots show an increase in SNR_T by $\approx$ +1dB from applying WDN. The benefits of this procedure are not immediately obvious in the time-domain. Wavelet decomposition using db20 wavelet at a depth of 10 levels.

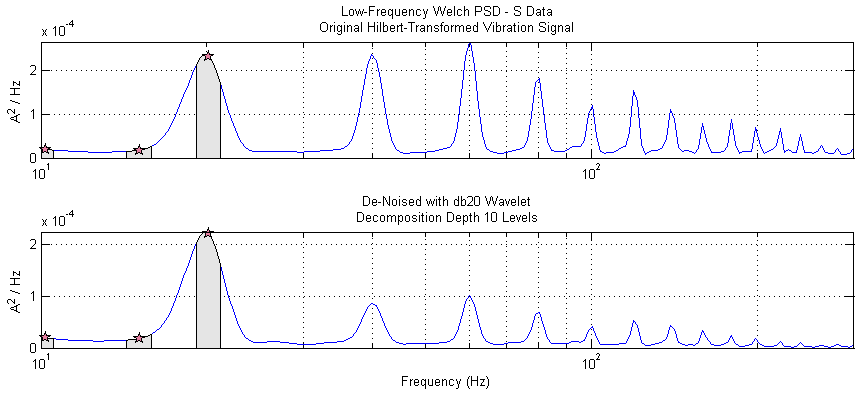

Figure 5.2: Welch PSD of signals shown in Figure 5.1 (before/after WDN). Gray area shows ±10% of possible frequencies

5.1.2 Time-Domain Detection

As described in Section 4.1.3, the ability to identify the fault in the time domain is tested. The signal is run through a peak detector and thresholded in the time domain. The confidence interval plot in Figure 5.3 shows the improvement in detection ability for a wider range of α. The bands around the estimate denote 95% confidence intervals. The histograms in Figures 5.4 and 5.5 demonstrate what happens as α becomes too high, and the time-domain plot in Figure 5.6 shows the location of the threshold for $\alpha = 46$.

5.1.3 Remarks

The WDN algorithm successfully attenuates non-fault related envelopes in the signal, increasing the probability of proper fault identification using both frequency-domain (PSD) and time-domain (peak thresholding) methods. The confidence interval plot in Figure 5.3 shows a "compression" in confidence with variation in threshold scaling α. In the sections that follow, these techniques are tested on real-world signals to verify results.

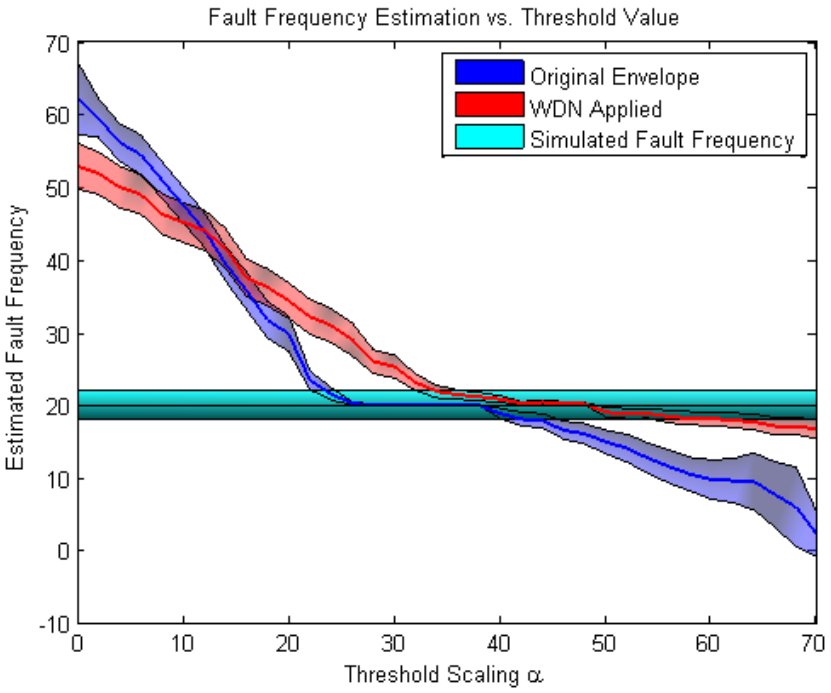

Figure 5.3: Estimated fault frequency vs. threshold level for the noisy pulse signal shown in 5.1, periodic at 20Hz. By thresholding the peaks of this envelope at a variable level α, the de-noised envelope signal is shown to more accurately reflect periodicity at the fault frequency.

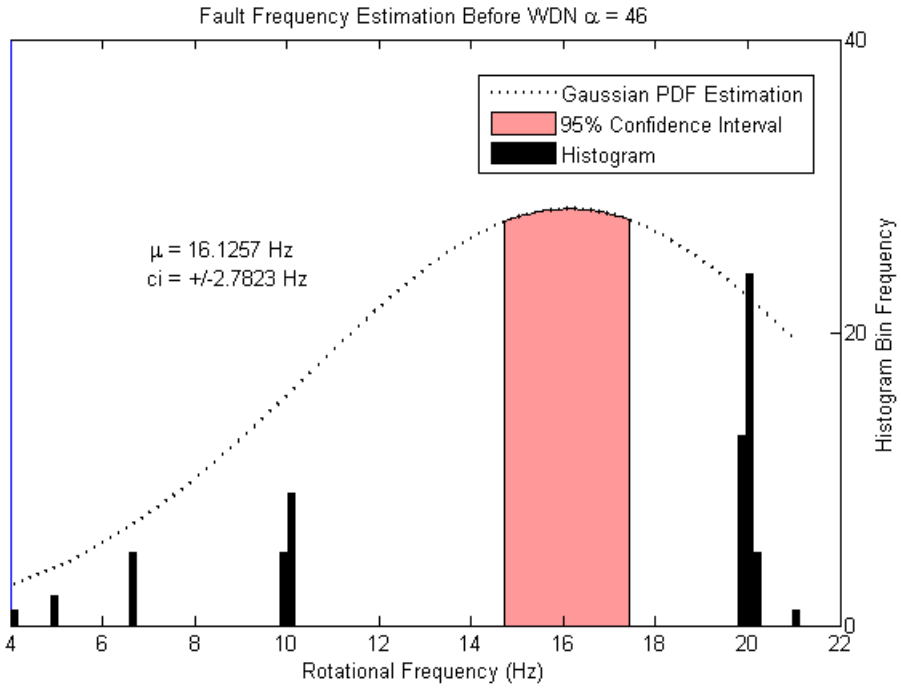

Figure 5.4: Histogram of impulse frequencies, before WDN. These values are derived from the threshold shown in Figure 5.6. Low frequency content is a result of the threshold missing lower-amplitude peaks.

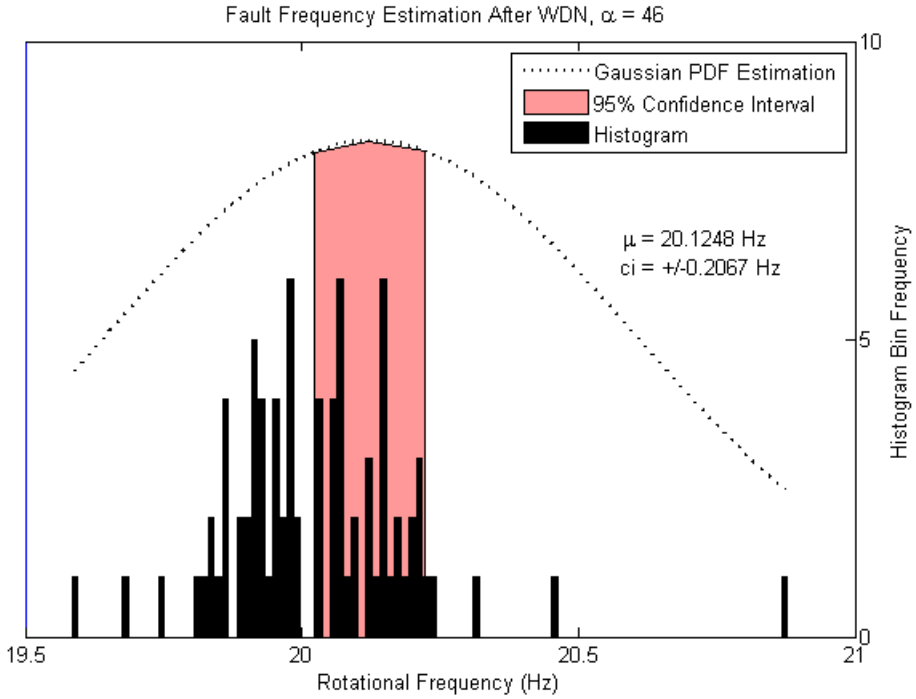

Figure 5.5: Histogram of impulse frequencies, after WDN. With the same threshold as Figure 5.4, more peaks are included in the measure, at the proper fault frequency (around 20Hz).

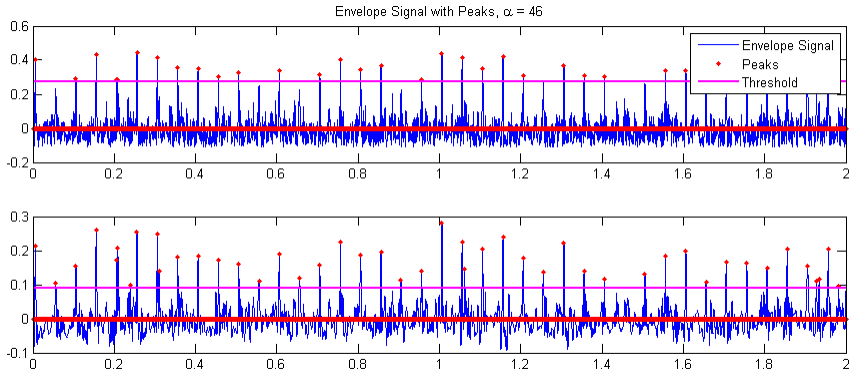

Figure 5.6: A threshold set too high results in peaks being discarded from the first plot, whereas the WDN version of the signal still contains these peaks.

5.2 DC MOTOR

The testbed described in 4.2.2 is run through the same procedure as the synthesized signal from the previous section. This provides real-world observations to confirm hypotheses from synthetic testing. A time-domain plot of a short section of signal is shown in Figure 5.7. The SNR_T measure is shown in Figure 5.8.

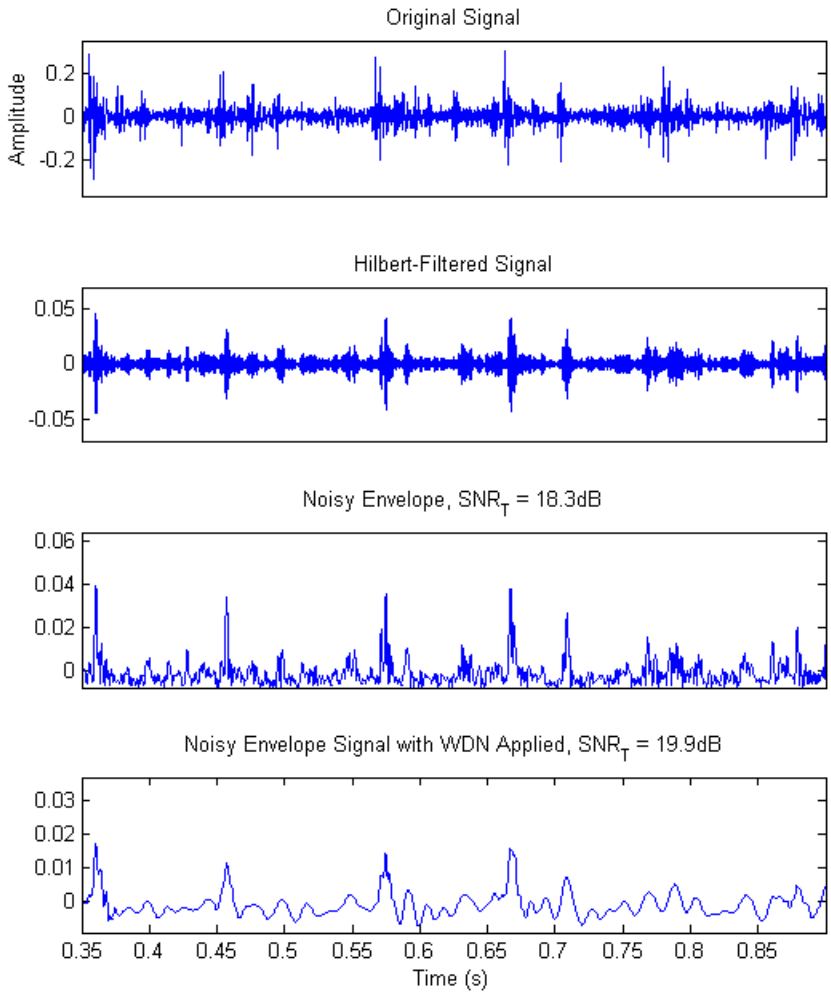

Figure 5.7: Time-domain waveform of DC-motor vibration signal at all stages of the algorithm.

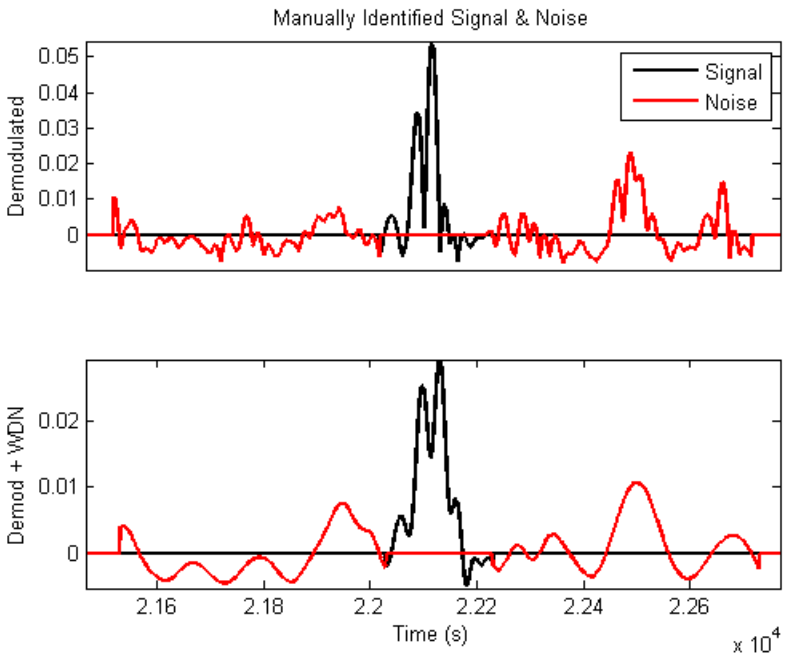

Figure 5.8: An isolated waveform peak. Before de-noising (top), $\text{SNR}_T \approx 18.3\text{dB}$. After de-noising (bottom), $\text{SNR}_T \approx 19.9\text{dB}$.

The db20 wavelet is used to de-noise at 6 levels of decomposition. Again using equations from Section 4.3.2, the resulting lowpass (scaling filter) cutoff is $\approx$ 78Hz. With a rotational speed of around 594 RPM (9.9Hz), the theoretical maximum fault frequency (BPFI) for the SR-12 bearing is approximately 55Hz. This ensures that none of the fault frequencies will fall between subbands. The improvement in SNR is around +1dB.

5.2.1 Frequency-Domain Detection

The low frequency PSD's (Figure 5.9) before and after WDN are nearly identical. The theoretical fault frequencies (BSF, BPFO, BPFI) are grey. The magnitude-squared energy at BPFI ($\approx$ 55Hz) dominates the spectrum.

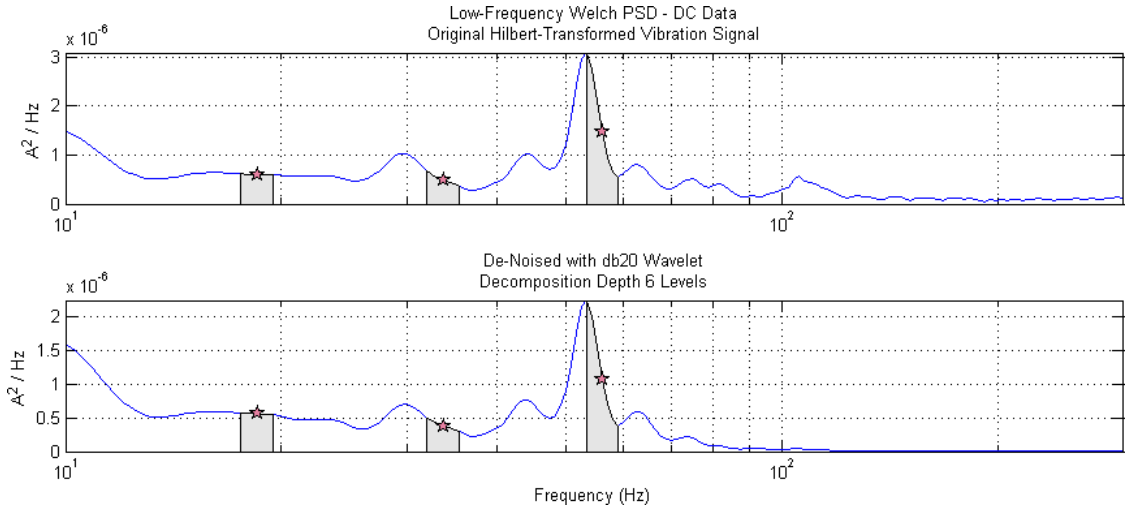

Figure 5.9: Welch PSD of signals shown in Figure 5.7 (before/after WDN). Gray area shows ±10% of possible fault frequencies

5.2.2 Time-Domain Detection

Improvement in time-domain identification is more pronounced. As with the synthetic signal experiment, the variation in accuracy with threshold α is "compressed" over a wider range. Figure 5.10 demonstrates this. With WDN applied (shown in red), good values of α include $\alpha = 1$, which means that this scaling factor is not actually necessary to identify faults properly.

5.2.3 Remarks

One possible source of error is RPM measurement, which is derived from an optical reflectivity sensor. The output is a square wave, and the total number of zero-crossings per recording session is the frequency of rotation. The true speed may actually vary within the recording. This may explain the deviation of the peak in Figure 5.9 from the theoretical fault frequency.

With a degree confidence, the assertion is that this SR-12 bearing contains a faulty inner-raceway. The in-band SNR in this experiment is relatively high, as seen in the

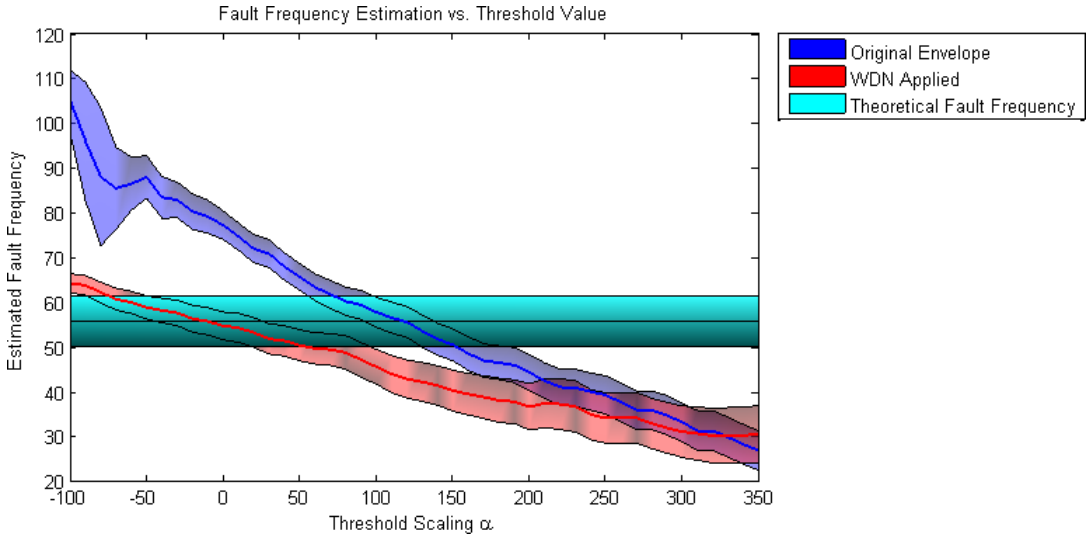

Figure 5.10: Estimated fault frequency vs. threshold level for the vibration signal shown in 5.7. By thresholding the peaks of this envelope at a variable level α, the de-noised envelope signal is shown to more accurately reflect periodicity at the fault frequency for lower variation in α.

PSD plot of Figure 5.9, so wavelet de-noising does not improve frequency-domain identification.

5.3 CASE WESTERN VIBRATION DATASET

This final experimentation tests the WDN algorithm with precisely seeded fault data. The smallest faults are 0.007", which will be shown in this report. A time-domain waveform is shown of the signal at all stages of the algorithm in Figure 5.11.

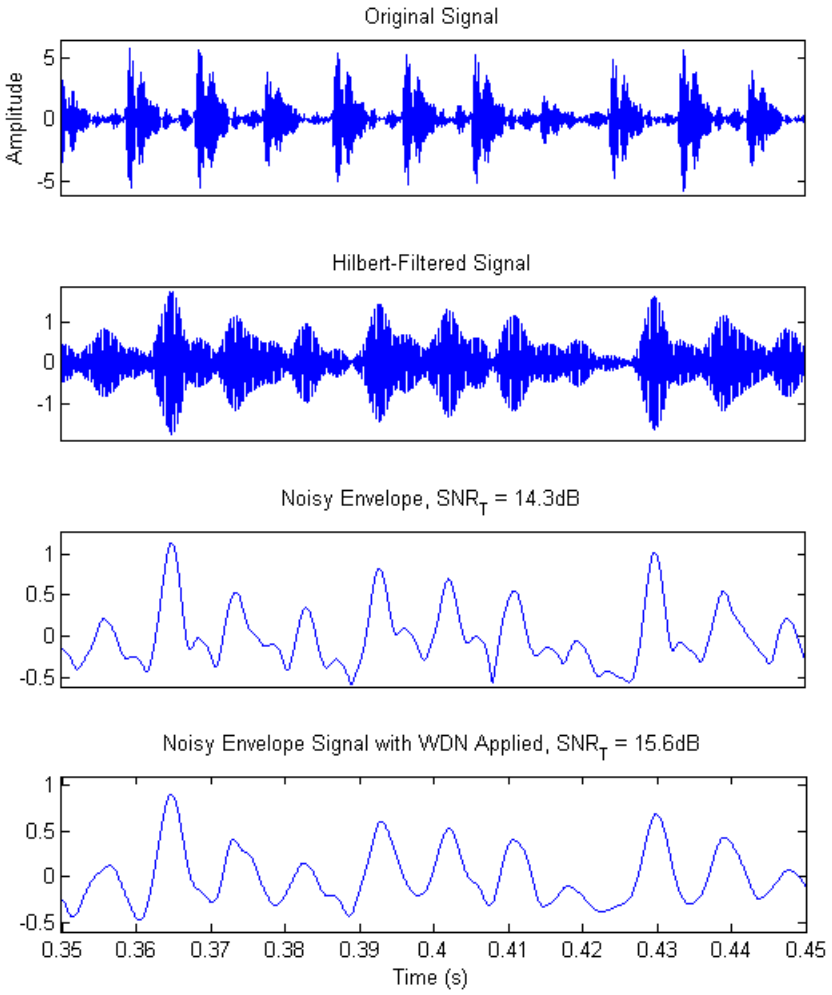

Figure 5.11: The time-domain waveform of a seeded fault with 0.007" diameter in the outer-raceway at all stages of the algorithm. Data from [12].

The db20 wavelet is used to de-noise at 7 levels of decomposition. The resulting lowpass (scaling filter) cutoff is $\approx$ 187Hz. With a rotational speed of around 1796 RPM (30Hz), the theoretical maximum fault frequency (BPFI) for the SKF 6205-2RS bearing is approximately 107Hz. The improvement in estimated SNR_T is negligible.

5.3.1 Frequency-Domain Results

The 0.007" outer raceway fault is distinguishable by the spectral peak in Figure 5.12. One noticeable improvement is the BPFO harmonic at $\approx$ 210Hz, marked in red in the figure, removed by WDN.

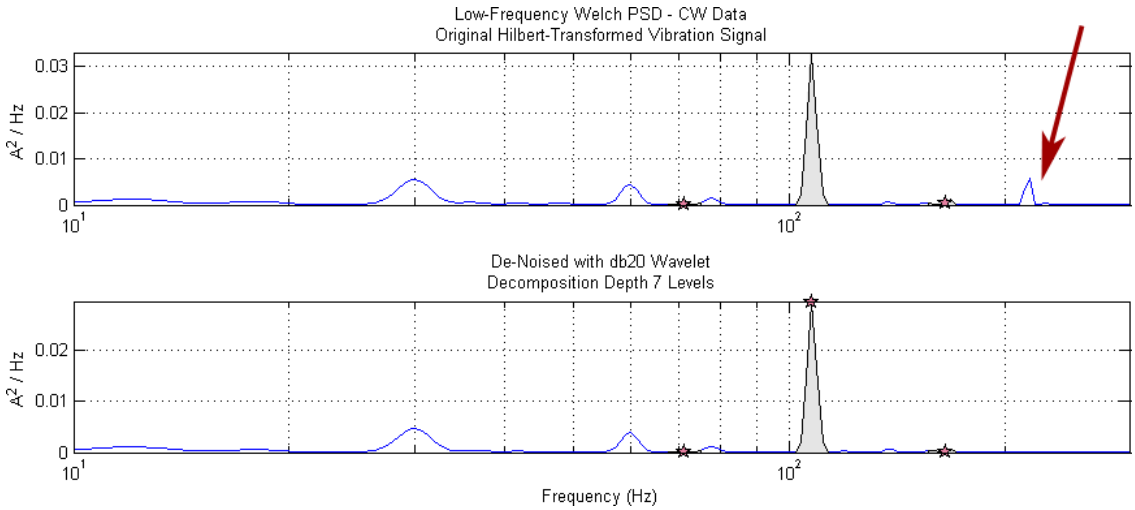

Figure 5.12: Low frequency PSD of the vibration signal shown in Figure 5.11. The fault frequency BPFO is approximately 107Hz.

5.3.2 Time-Domain Results

The removal of the 210Hz harmonic has implications when attempting to identify faults in the time-domain. Figure 5.13 shows that the threshold method may pick up this harmonic as the dominant envelope peak frequency. This issue arises when dealing with the BPFO and BSF, since their second harmonics are near BPFI. As α

increases, the estimation becomes accurate for the non de-noised signal, where the de-noised signal works well into negative values. At large negative values of α, the algorithm is simply measuring the distance between *all* peaks.

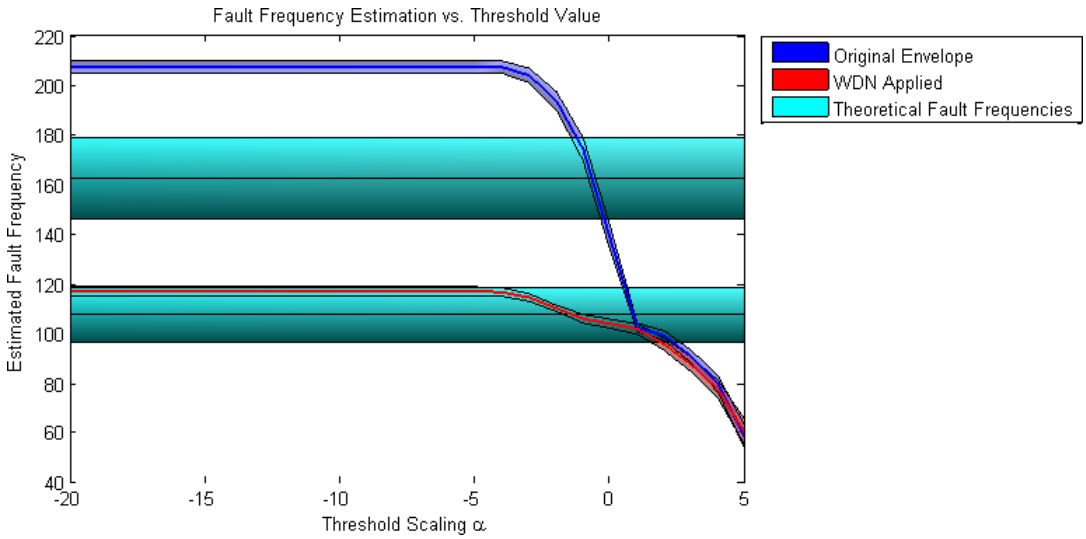

Figure 5.13: Estimated fault frequency vs. threshold level for the vibration signal shown in 5.11. This figure demonstrates the importance of removing in-band harmonics from envelope signals.

5.3.3 Remarks

WDN successfully improved the time-domain fault identification method by reducing its dependence on α. Other datasets from [12] were tested, with similar results.

Chapter 6

Conclusions

In this thesis, we have presented a method to improve detection confidence in fault identification using wavelet de-noising. The method deals with the myriad of in-band noise sources in narrowband vibration signals without *a priori* noise statistics.

Decomposition techniques are more suitable to detecting smooth signals, therefore, WDN is applied after envelope demodulation. This yields better results than attempting to de-noise a broadband vibration signal, as in [6].

For general purpose signal conditioning, wavelet de-noising is a low-risk, widely applicable technique. Donoho [3] proves that the gains in noise reduction outweigh the costs of removing low-energy details from the signal. Therefore, unless computational limitations are critical, there is little reason not to utilize such an algorithm.

While this thesis demonstrates the function of WDN in the context of demodulated vibration signals, it also serves as a guide for parameter choice. The number of parameters that control this algorithm can be unwieldy, but some sensible decisions and simplifying assumptions allow for ease of use:

- ϕ – wavelet type – In this thesis, we decide upon the Daubechies wavelet for its flat passband characteristics. This choice allows for accurate representation of signal proportions in the scale-space domain. In our experiments, the db20 wavelet is sufficient. We choose a high order wavelet, so that the passband cutoff is sharp. This allows for a high number of decompositions without compromising the amplitudes of coefficients in the lower passbands.

- λ – soft threshold level – This value was derived by Donoho [3] to be a function of noise variance, which is unknown. We simplify this choice by assuming the in-band noise is white, so that the resulting threshold is a function of signal variance, which is known.

- n_d – decomposition level – For our applications, we are searching for energy in the baseband (a demodulated AM-signal). The maximum frequency of a bearing fault is the inner raceway fault frequency (BPFI). Therefore, the decomposition level must not be so high as to place the lowest subband cutoff below this frequency.

6.1 FUTURE WORK

To carry this research one step further, it is recommended that power levels be trended over long timescales. The improvements provided by WDN have yet to be tested for evaluation of Remaining Useful Life (RUL). It may be hypothesized that, due to the early-detection and confidence improvements demonstrated in this thesis, any RUL measure will benefit from earlier, more accurate fault specifics.

With reference to those algorithms tested by Qui et al. [6], a direct comparison between wavelet filtering and WDN was never performed, but may be warranted. The WDN algorithm as presented in this thesis requires minimal interaction to improve results, where wavelet filtering requires some recursion to tune parameters. Their relative speeds and effectiveness are a worthwhile measurement.

Another possible direction is testing the improvements in machine-learning algorithms for detecting/identifying faults. WDN refines the envelope analysis measure, therefore any system that utilizes envelope analysis methods will benefit from the added WDN processing.

One final possibility is the expansion of work discussed in Section 2.2.4. The wavelet transform is shown in [18] to directly demodulate a bandpass signal, via its modulus. Therefore, the demodulation and de-noising steps may be combined into a single transformation.

APPENDIX A
DAUBECHIES WAVELETS

These wavelets are compactly supported (FIR), maximally-flat, and orthogonal. The shortest filter is the Haar basis, shown in Figure A.1. As the number of coefficients increases, the filter cutoff becomes sharper. From a multiresolution analysis standpoint, this implies less spectral leakage between subbands. The db6 and db20 wavelet, shown in Figures A.3 and A.5, have increasingly better subband isolation properties.

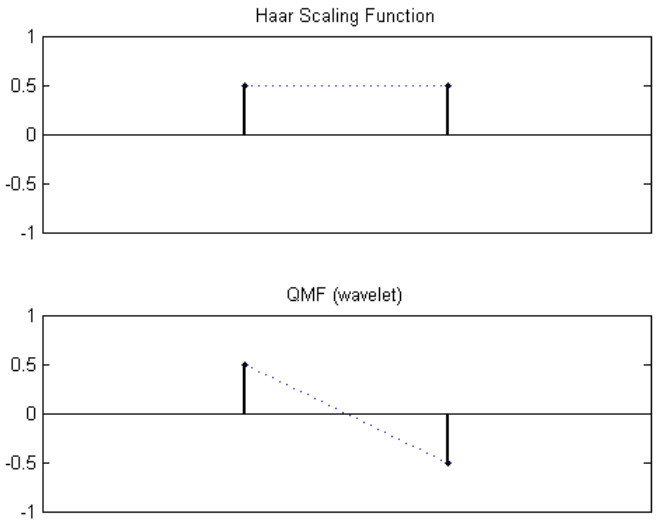

Figure A.1: Haar wavelet.

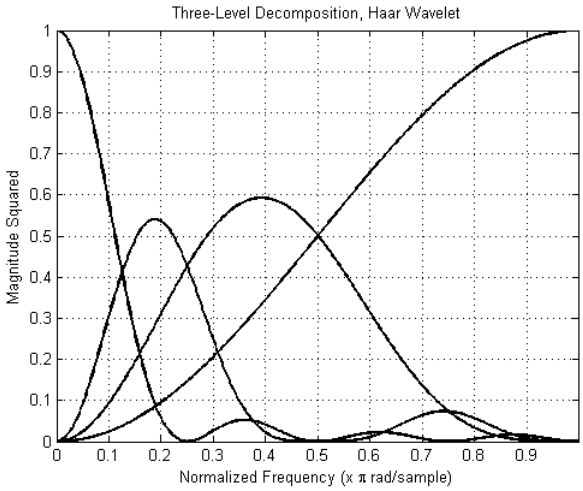

Figure A.2: Magnitude-squared response of a 3-level decomposition using the Haar basis.

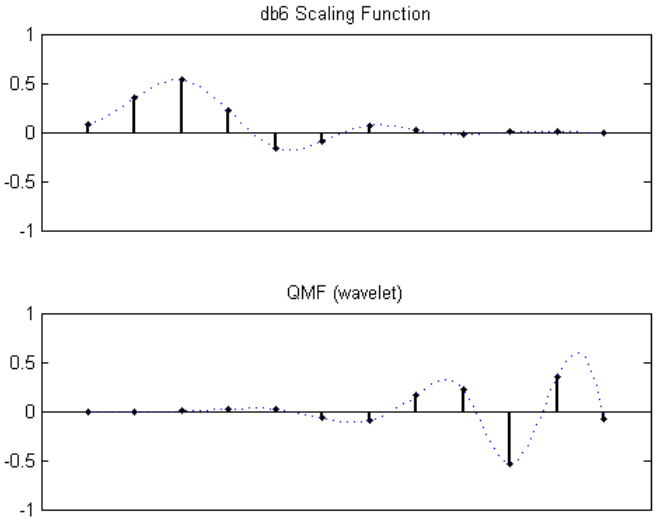

Figure A.3: db6 wavelet.

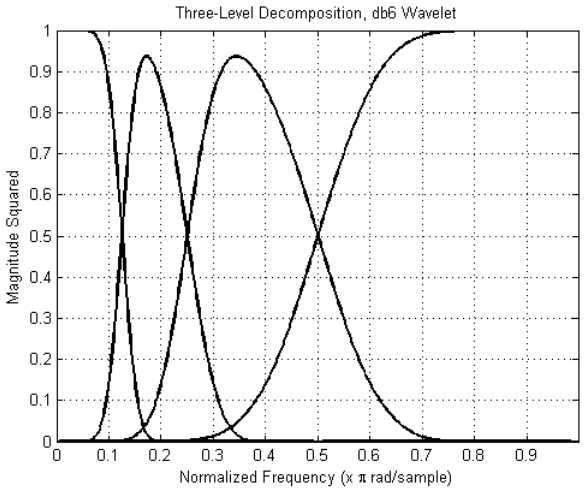

Figure A.4: db6 magnitude-squared response.

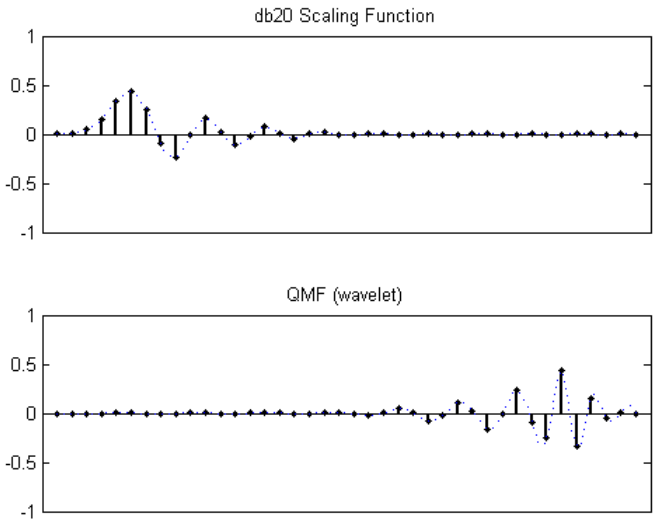

Figure A.5: db20 wavelet.

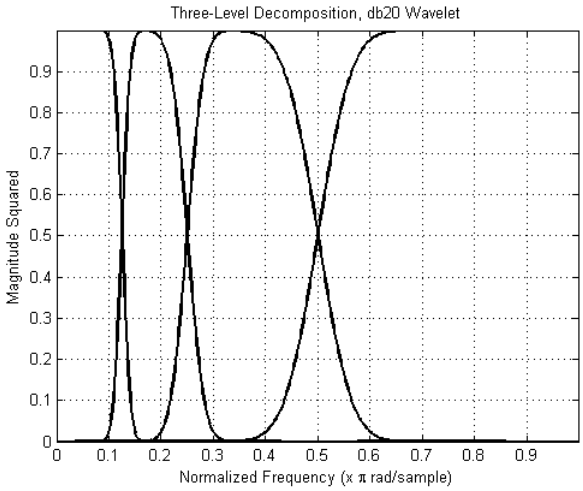

Figure A.6: db20 magnitude-squared response.

APPENDIX B

FILTER DESIGN FOR ENVELOPE DEMODULATION

The following code uses the MATLAB Filter Design Toolbox to create a bandpass filter for use in envelope demodulation, as discussed in Chapter 4.

```
bw = fc/5;
tw = bw/2;


fp1 = fc-bw/2;  % Lower edge of passband (Hz)
fp2 = fc+bw/2;  % Upper edge of passband (Hz)
fst1 = fp1-tw;  % Lower edge of stopband (Hz)
fst2 = fp2+tw;  % Upper edge of stopband (Hz)
ast1 = 60;      % Attenuation in the first stopband (dB)
ast2 = 60;      % Attenuation in the second stopband (dB)
ap = 1;         % Amount of ripple allowed in the passband (dB)


d = fdesign.bandpass(fst1,fp1,fp2,fst2,ast1,ap,ast2,fs);
```

`fc` is defined as the structure's vibrational mode of interest, `bw` is the filter bandwidth, and `tw` is the cutoff transition width. See the `fdesign.bandpass` help file for more information.

APPENDIX C

TEST PLATFORMS AND EQUIPMENT

Two real-signal data sets are used in the overall testing process.

- Published vibration data available from [12]. Figure C.1.
- A small DC motor driving a bearing. Figure C.2.

For each platform, the general methodology is similar. The vibration sensor(s) is strategically placed on the platform, preferably in close proximity to bearings. The platform is operated with both new and faulty bearings, at various speeds. This is an attempt to simulate as many real-world operational scenarios as possible. All test platforms are equipped with a means of measuring rotational speed.

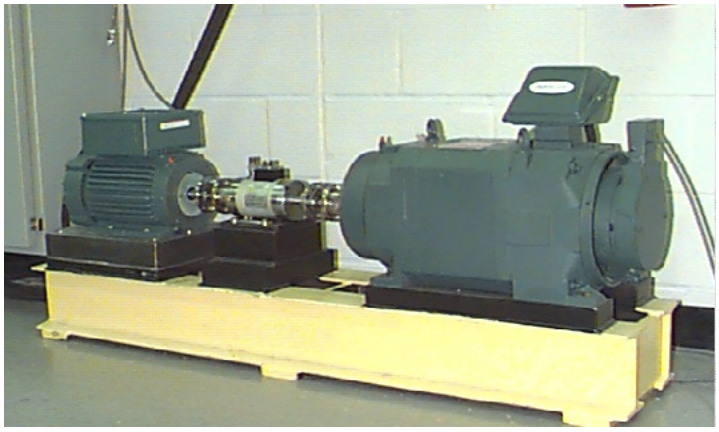

Figure C.1: Published data setup from [12].

The bearing used in the Case-Western experiment is the SKF 6205-2RS single row ball bearing, with the following dimensions (in mm):

$$d_b = 0.3126$$

$$n_{balls} = 9$$

$$phi = 0$$

$$d_p = 1.537$$

For the DC motor experiment, the KML SR12-2RS bearing is used, with identical dimensions to the more common SKF 98204 Y (in mm):

$$d_b = 7.8$$

$$n_{balls} = 9$$

$$phi = 0$$

$$d_p = 31$$

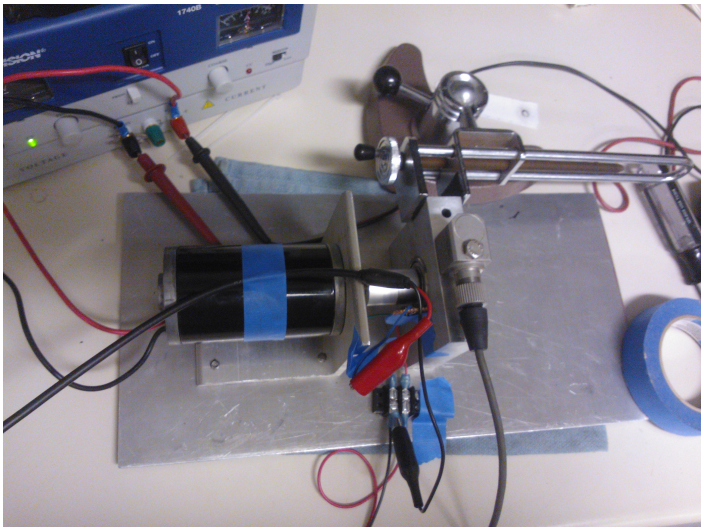

Figure C.2: DC motor test platform.

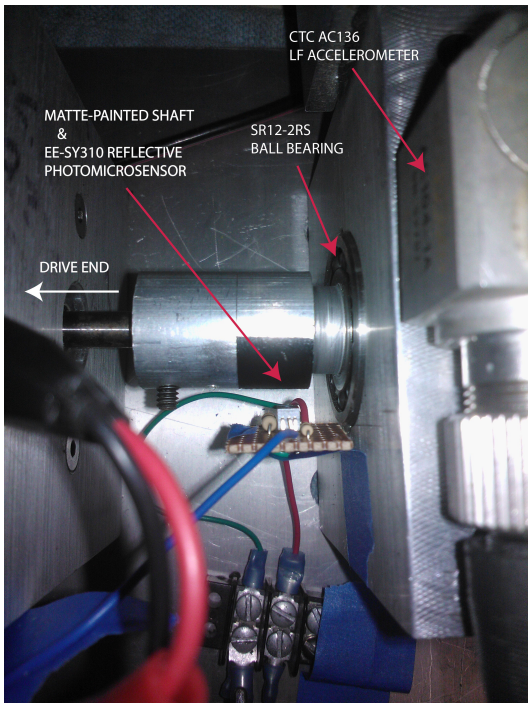

Figure C.3: Close-up view of RPM sensor, vibration sensor, bearing, and drive shaft.

BIBLIOGRAPHY

[1] S. Mallat and W. L. Hwang. "Singularity Detection and Processing with Wavelets." *IEEE Transactions on Information Theory.* vol. 38, no. 2, pg 617-643, 1992.

[2] D. L. Donoho and I. M. Johnstone. "Ideal Spatial Adaptation via Wavelet Shrinkage." *Biometrika.* vol. 81, pg. 425-455, 1994.

[3] D. L. Donoho. "De-Noising by Soft-Thresholding." *IEEE Transactions on Information Theory.* vol. 41, no. 3, pg. 613-627, 1995

[4] I. Daubechies. *Ten Lectures on Wavelets.* Philadelphia, PA: Society for Industrial and Applied Mathematics, 1992. Print.

[5] A. Akansu and R. Haddad. *Multiresolution Signal Decomposition: Transforms, Subbands, and Wavelets.* Boston: Academic, 1992. Print.

[6] H. Qiu, J. Lee, J. Lin, and G. Yu. "Wavelet Filter-Based Weak Signature Detection Method and its Application on Rolling Element Bearing Prognostics." *Journal of Sound and Vibration.* vol. 289, pg. 1066-1090, 2006.

[7] N. Waters and P. Beaujean. "Targeting Faulty Bearings for an Ocean Turbine Dynamometer." *International Journal of Prognostics and Health Monitoring.* vol. 4, pg 1-15, 2013.

[8] R. Wald, T. Khoshgoftaar, and J. Sloan. "Using Feature Selection to Determine Optimal Depth for Wavelet Packet Decomposition of Vibration Signals for Ocean System Reliability." *Unpublished.* 2014

[9] P. McFadden and J. Smith. "Model for the vibration produced by a single point defect in a rolling element bearing." *Journal of Sound and Vibration.* vol. 96, no.1, pg 69-82, 1984.

[10] O. Rioul and M. Vetterli. "Wavelets and signal processing." *IEEE Signal Processing Magazine.* vol.8, no.4, pg. 14-38, Oct. 1991.

[11] I. S. Bozchalooi and M. Liang. "A Combined Spectral Subtraction and Wavelet De-Noising Method for Bearing Fault Diagnosis." *IEEE Proceedings of the 2007 American Control Conference.* pg. 2533-2538, July 11-13, 2007.

[12] Bearing Data Center, Seeded Fault Test Data. (Unknown Authors) *Case Western Reserve University, Rockwell Science Center, Office of Naval Research.* Web. Retrieved January 2014. <http://csegroups.case.edu/bearingdatacenter/>

[13] L. Eren and M. Devaney. "Bearing Damage Detection via Wavelet Packet Decomposition of the Stator Current." *IEEE Transactions on Instrumentation and Measurement.* vol. 53, no. 2, pg. 431-436, 2004.

[14] J. P. Dron, F. Bolaers, Rasolofondraibe. "Improvement of the Sensitivity of the Scalar Indicators (Crest Factor, Kurtosis) Using a De-Noising Method by Spectral Subtraction: Application to the Detection of Defects in Ball Bearings." *Journal of Sound and Vibration.* vol. 270, no. 1-2, pg. 61-73, 2004.

[15] B. Widrow, et al. "Adaptive Noise Cancelling: Principles and Applications." *Proceedings of the IEEE.* vol. 63, no. 12, pg. 1692-1716, 1975.

[16] N. Waters. *Detection, localization, and identification of bearings with raceway defects for a dynamometer using high frequency modal analysis of vibrations across an array of accelerometers.* Thesis, Florida Atlantic University, 2012. Print.

[17] P. Gendron and B. Nandram. "Modeling Heavy-Tailed Correlated Noise with Wavelet Packet Basis Functions." *Journal of Statistical Planning and Inference.* vol. 112, pg. 99-114, 2003.

[18] N. G. Nikolaou and I. A. Antoniadis. "Demodulation of Vibration Signals Generated by Defects in Rolling Element Bearings Using Complex Shifted Morlet Wavelets." *Mechanical Systems and Signal Processing* vol. 16, no. 4, pg. 677-694, 2002.

[19] C. Taswell. "Randomized Signal Classes for Evaluating the Performance of Wavelet Shrinkage Denoising Methods." *Proceedings of the International Association of Science and Technology Conference, Signal and Image Processing (SIP'99).* October 18-21, 1999.

[20] M. Mjit. *Methodology for fault detection and diagnostics in an ocean turbine using vibration analysis and modeling.* Thesis, Florida Atlantic University, 2009. Print.